Illuminating a tadpole's metamorphosis II: observing the ongoing transformation with ALMA

Megan Reiter [1]★ Andrés E. Guzmán [2] Thomas J. Haworth [3]
Pamela D. Klaassen [1] Anna F. McLeod,[4,5] Guido Garay[6] and Joseph C. Mottram[7]

[1]*UK Astronomy Technology Centre, Blackford Hill, Edinburgh EH9 3HJ, UK*
[2]*National Astronomical Observatory of Japan, 2-21-1 Osawa, Mitaka, Tokyo 181-8588, Japan*
[3]*Astronomy Unit, School of Physics and Astronomy, Queen Mary University of London, London E1 4NS, UK*
[4]*Department of Astronomy, University of California Berkeley, Berkeley, CA 94720, USA*
[5]*Department of Physics and Astronomy, Texas Tech University, PO Box 41051, Lubbock, TX 79409, USA*
[6]*Departamento de Astronomía, Universidad de Chile, Camino el Observatorio 1515, Las Condes, Santiago, Chile*
[7]*Max Planck Institute for Astronomy, Königstuhl 17, D-69117 Heidelberg, Germany*

ABSTRACT

We present new Atacama Large Millimeter/submillimeter Array observations of the tadpole, a small globule in the Carina Nebula that hosts the HH 900 jet+outflow system. Our data include ^{12}CO, ^{13}CO, C^{18}O $J=2$–1, ^{13}CO, C^{18}O $J=3$–2, and serendipitous detections of DCN $J=3$–2 and CS $J=7$–6. With angular resolution comparable to the *Hubble Space Telescope*, our data reveal for the first time the bipolar molecular outflow in CO, seen only inside the globule, that is launched from the previously unseen jet-driving protostar (the HH 900 YSO). The biconical morphology joins smoothly with the externally irradiated outflow seen in ionized gas tracers outside the globule, tracing the overall morphology of a jet-driven molecular outflow. Continuum emission at the location of the HH 900 YSO appears to be slightly flattened perpendicular to outflow axis. Model fits to the continuum have a best-fitting spectral index of ∼2, suggesting cold dust and the onset of grain growth. In position–velocity space, ^{13}CO and C^{18}O gas kinematics trace a C-shaped morphology, similar to infall profiles seen in other sources, although the global dynamical behaviour of the gas remains unclear. Line profiles of the CO isotopologues display features consistent with externally heated gas. We estimate a globule mass of ∼1.9 M$_\odot$, indicating a remaining lifetime of ∼4 Myr, assuming a constant photoevaporation rate. This long globule lifetime will shield the disc from external irradiation perhaps prolonging its life and enabling planet formation in regions where discs are typically rapidly destroyed.

Key words: H II regions – (ISM): jets and outflows – (ISM:) individual: NGC 3372 – photodissociation region (PDR) – stars: formation.

1 INTRODUCTION

Ionizing radiation permeates high-mass star-forming regions, sculpting the natal cloud and excavating newly born stars. On large scales, ionizing radiation clears low-density gas, contributing to the ultimate destruction of the cloud and possibly resupplying turbulence (e.g. Gritschneder et al. 2009, 2010; Dale & Bonnell 2011; Dale, Ercolano & Bonnell 2013; Tremblin et al. 2013; Walch et al. 2013; Boneberg et al. 2015; Dale 2017). Feedback also affects the much smaller scales of individual stars and their circumstellar

(planet-forming) discs (e.g. Mann et al. 2014; Winter et al. 2018; Nicholson et al. 2019).

In between these two extremes are small ($r < 1$ pc), bright-rimmed clouds often seen in and around H II regions (e.g. Smith, Bally & Morse 2003; Gahm et al. 2007; Wright et al. 2012). Some appear to harbour nascent protostars (e.g. McCaughrean & Andersen 2002; Sahai, Güsten & Morris 2012a; Reiter et al. 2015b), while others appear to have resisted collapse (e.g. Smith, Barbá & Walborn 2004; Gahm et al. 2013; Haikala et al. 2017). Mass estimates for these globules range from planetary to stellar masses (Gahm et al. 2007; Sahai et al. 2012a; Gahm et al. 2013; Haikala et al. 2017). Several theoretical models have explored how external irradiation affects the globules, including whether

★ E-mail: megan.reiter@stfc.ac.uk
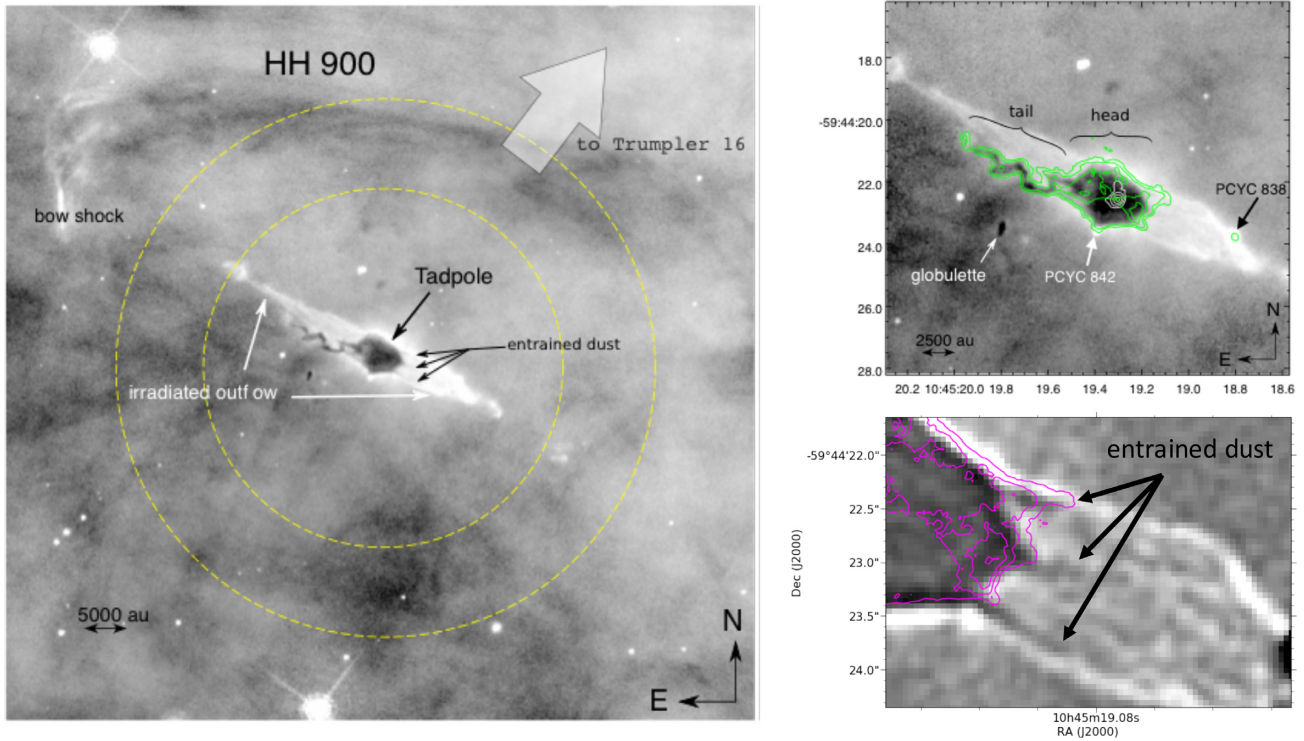
Figure 1. ACS/*HST* H α image of the tadpole (Reiter et al. 2015b). Left: Field of the tadpole. Dashed circles indicate the FWHM of Band 6 and 7 primary beams. Right: White contours show ALMA continuum emission at 233 GHz (levels: 0.52, 0.78, 1.3, and 2.1 mJy beam^{-1}). Green contours show CO $J=2–1$ integrated over $[-57, -11]$ km s^{-1}. Intermediate contours display the bipolar outflow pattern of emission detected towards the tadpole (levels: 20, 50, 120, and 180 K km s^{-1}). Bottom right: A zoom on the globule with an unsharp mask applied to emphasize the three dust streamers (labelled). Magenta contours are the CO $J=2–1$ integrated intensity, as above.

it may stimulate collapse through radiatively driven implosion (RDI; e.g. Bertoldi 1989; Lefloch & Lazareff 1994; Kessel-Deynet & Burkert 2003; Miao et al. 2009; Bisbas et al. 2011; Haworth et al. 2013). If stimulated to collapse, small globules may contribute significantly to the low-mass end of the initial mass function.

Small, opaque globules are typically identified in images where they are seen in silhouette against the bright background of the H II region. Most studies use narrow-band optical images as these provide higher angular resolution than single-dish observations at the long wavelengths that probe cold, molecular gas (Bok 1948; Pottasch 1956, 1958; Dyson 1968; Herbig 1974; Schneps, Ho & Barrett 1980; Reipurth 1983; Gahm et al. 2007; Wright et al. 2012; Grenman & Gahm 2014). More recent efforts have targeted some larger globules for millimetre observations to measure molecular gas masses and radial velocities. Beam sizes from these single-dish studies tend to be significantly larger than the globules themselves, so bulk properties are inferred from line ratios and profiles (e.g. Sahai et al. 2012a; Gahm et al. 2013; Haikala et al. 2017). Determining how feedback affects the fate of small globules requires spatially and spectrally resolved observations of the structure and kinematics of the cold molecular gas.

The subject of this study is a small globule in the Carina Nebula, which we colloquially refer to as the tadpole (see Fig. 1). Multiple O-type stars in the nearby cluster Tr16 illuminate the globule and the peculiar HH 900 jet+outflow system that emerges from it (Smith, Bally & Walborn 2010). With a jet dynamical age of ~2200 yr (Reiter et al. 2015b), HH 900 is one of the youngest jets in Carina. Derived jet kinematics require a driving source

embedded in the small opaque globule, but previous observations provided no evidence for a protostar inside the tadpole. Even at shorter wavelengths (i.e. 3.6 μm with *Spitzer*), the angular resolution is comparable to the size of the globule, making it difficult to distinguish between emission from an embedded source and the two protostars that lie just outside the globule (see Fig. 1). Confusion only worsens towards longer wavelengths (with e.g. *Herschel*) where young (Class 0) protostars emit the majority of their radiation. At the southern declination of Carina, only the Atacama Large Millimeter/submillimeter Array (ALMA) provides the requisite angular resolution to detect an embedded protostar and the structure and kinematics of the surrounding globule.

A word on terminology: We use 'outflow' to describe wide-angle flows that may be ambient material entrained by the jet or may originate from the disc wind (see e.g. Klaassen et al. 2015). These typically trace slower emission, with velocities of ~10s of km s^{-1}, and are often observed in molecular gas tracers like CO, but in highly irradiated regions like Carina, may also be seen in ionized gas tracers like H α (see e.g. Reiter et al. 2015a, b). This is different from the 'jet' that we use to refer to the fast (~100 km s^{-1}), collimated (opening angles <10°) stream of emission most often seen in the optical and near-IR.

In Reiter et al. (2019), hereafter Paper I, we presented optical integral field-unit spectroscopy of the tadpole from the Multi Unit Spectroscopic Explorer on the Very Large Telescope. Physical properties derived from optical diagnostics probe the conditions in the ionized and partially neutral gas on the surface of the globule and in the externally irradiated jet+outflow system. Combining these diagnostics with spatially resolved observations of the kinematics

Table 1. ALMA observation parameters.

Band	Pha. cal. flux (mJy)	Observation date (dd-mm-yyyy)	t_{on} (s)	MAR[a] (arcsec)	MRS[b] (arcsec)
6	560.7	08-05-2017	912	0.24	10.7
	564.5	25-09-2017	3008	0.02	3.9
7	502.2	31-10-2016	910	0.17	6.0

Notes. [a]MAR = maximum angular resolution.
[b]MRS = maximum recoverable scale, given by $0.6\lambda/L_{min}$.

in the cold molecular gas provides a powerful probe of how the environment affects the evolution of small globules.

In this paper (Paper II), we present spatially and spectrally resolved ALMA observations of the cold, molecular gas in the tadpole. Unlike previous observations of the molecular content of small globules, our ALMA data have angular resolution comparable to the *Hubble Space Telescope (HST)*, allowing us to detect the jet-driving source and the associated molecular outflow for the first time. Comparing the physical properties of the cold molecular gas derived here with the impact of the environment determined from optical IFU spectroscopy (Paper I), we will quantify how feedback from the high-mass star-forming environment determines the fate of this small globule (Reiter et al. 2020; Paper III).

2 OBSERVATIONS

ALMA Band 7 and 6 observations of the HH 900 globule were obtained in 2016 and 2017, respectively. Table 1 lists observational parameters including the derived flux of the phase calibrator J1047−6217, the date of the observations, the on-source time, the maximum angular resolution (MAR; given by λ/L_{max}, where L_{max} is the largest baseline), and the maximum recoverable scale [MRS; given by $0.6\lambda/L_{min}$, where L_{min} is the shortest baseline; see equation (3.28) in Remijan et al. (2019)]. Observations consisted of 12 m-array (40 antennae) single pointing scans towards R.A.=$10^h45^m19^s.3$, decl.=$-59°44'23''.0$ (ICRS). Band 6 observations were taken using a medium (L_{max} = 1.1 km, C40-5) and long baseline (L_{max} = 14.9 km, C40-8) configuration, while Band 7 was observed using only the medium baseline configuration (C40-5). The field-of-view full width at half-maximum (FWHM) of Bands 6 and 7 is 27 and 19 arcsec, respectively.

Our spectral set-up targeted rotational transitions J=2–1 and 3–2 of the CO isotopologues ^{13}CO and $C^{18}O$, as well as ^{12}CO J=2–1 and SiO J=5–4 in the Band 6 set-up. We observed ^{13}CO and $C^{18}O$ lines with velocity resolution ranging between 0.06 km s^{-1} at Band 7 and 0.08 km s^{-1} at Band 6. The main CO isotopologue and the SiO line were observed with 0.16 and 0.34 km s^{-1} velocity resolution, respectively. We also observed continuum spectral windows with resolution between 1.7 and 2.5 km s^{-1} covering approximately 4 and 6 GHz in Bands 6 and 7, respectively. Bandpass, flux, and gain calibration against external calibrators were done using the *Common Astronomy and Software Applications* (CASA; McMullin et al. 2007) v4.7. Bandpass and flux calibrators for the Band 6 observations performed in 2017 September were J0635−7516 and J0538−4405, respectively, while a single source, J1107−4449, was used for the 2017 May observations. Bandpass and flux calibrators for Band 7 observations were J0538−4405 and J1037−2934, respectively. Fluxes of the flux calibrators were interpolated from measurements performed by the ALMA calibrator survey separated from our project by less than 2 d. The fluxes derived for the bandpass calibrators (when it is not the flux calibrator) are within ∼2 per cent

compared with the values given by the ALMA calibrator survey (taken within 3 d from our observations) in all cases. Imaging and self-calibration was performed using CASA v5.4. Band 6 images were obtained using `tclean` by combining the data from both configurations in Table 1. Absolute flux scaling uncertainty is estimated to be about 15 per cent.

The synthesized beam sizes of the reduced data are given in Table 2 and range typically between $0''.1$ and $0''.2$, providing an excellent complement to Hα images obtained with *HST* (see Reiter et al. 2015b) and corresponding to a spatial resolution of 230–460 au at the distance of Carina (2.3 kpc; Smith 2006). We describe how we resolve the discrepancy in the ALMA and *HST* astrometry in Appendix A.

3 RESULTS AND ANALYSIS

With the superior sensitivity and angular resolution of ALMA, we resolve the structure and kinematics of the cold molecular gas associated with HH 900 jet+outflow system and the tadpole globule for the first time (see Fig. 2). Our ALMA observations have angular resolution comparable to *HST*, allowing the most direct comparison with the physical structures seen at shorter wavelengths (e.g. Paper I).

ALMA provides the first look inside the tadpole. We detect the previously unseen HH 900 jet-driving source (the HH 900 YSO; see Section 3.6). These data reveal the bipolar molecular outflow emerging from the HH 900 YSO that smoothly joins the irradiated outflow at the edge of the globule (see Figs 1 and 5). In addition, the largest angular scale of the ALMA observations includes a few features with associated molecular emission located outside the tadpole. We detect both continuum and CO emission from the young stellar object (YSO) that lies in the western limb of the irradiated outflow, PCYC 838 (see Fig. 1 and Appendix C). A small globulette, located just south of the tadpole tail, can be seen in silhouette against the background nebulosity and in emission in ^{12}CO (see Fig. 2). Molecular line data include the serendipitous detection of DCN J=3–2, and CS J=7–6. In the following sections, we derive the physical properties of these elements of the tadpole and HH 900 jet+outflow system.

3.1 Optical Depth

We have observed multiple isotopologues of CO, allowing us to calculate the optical depth at each position and velocity where emission is significantly detected (see Fig. 2) as follows:

$$\frac{T_{main,v}}{T_{iso,v}} = \frac{1-e^{-\tau_{main,v}}}{1-e^{-\tau_{iso,v}}} = \frac{1-e^{-\tau_{main,v}}}{1-e^{-\tau_{main,v}/R}}, \tag{1}$$

where we denote the more abundant species as 'main' and the optically thin transition used to correct it as 'iso' and assume that the excitation temperature is the same for both molecules. To compare the brightness temperature of the CO isotopologues, we convolve each map to the same resolution. The scale factor R is the relative abundance of the two species; we assume [CO/^{13}CO]=68 ± 20 and [CO/$C^{18}O$]=570 ± 130 at the Galactocentric radius of Carina of 8.1 kpc (Wilson 1999). The brightness temperature ratios T_{12}/T_{13} and T_{12}/T_{18} (corresponding to ^{12}CO/^{13}CO and ^{12}CO/$C^{18}O$ emission ratios, respectively) are both low ($\lesssim$4) throughout the globule, indicating that ^{12}CO is very optically thick.

Given the high optical depth in the ^{12}CO line, we also compute the optical depth of ^{13}CO by comparing the brightness temperature

Table 2. Spectral and imaging characteristics of the data.

Name	Frequency (GHz)	Bandwidth (MHz)	Resolution (km s^{-1})	θ_{min} (arcsec)	θ_{max} (arcsec)	P.A. (°)	RMS (mJy bm^{-1})	Comment
Molecular lines								
SiO J=5–4	217.104 9800	468.75	0.337	0.099	0.101	− 62.2	1.08	–
DCN J=3–2	217.2384	468.75	0.337	0.099	0.101	− 62.6	1.22	in SiO spectral window
C^{18}O J=2–1	219.560 3568	117.19	0.083	0.099	0.101	− 75.5	2.14	–
^{13}CO J=2–1	220.398 6765	117.19	0.083	0.097	0.126	− 81.3	2.69	–
^{12}CO J=2–1	230.538	234.375	0.159	0.096	0.103	− 77.4	2.41	–
C^{18}O J=3–2	329.330 5453	117.19	0.056	0.202	0.244	− 26.8	12.0	–
^{13}CO J=3–2	330.587 9601	117.19	0.055	0.201	0.240	− 27.1	10.2	–
CS J=7–6	342.882 8503	1875.0	1.71	0.209	0.225	− 35.4	2.69	–
Continuum								
B6 LSB	217.1	468.75	0.337	0.162	0.185	− 58.7	0.054[a]	SiO and DCN lines
B6 USB	232.2	1875.0	2.51	0.187	0.22	− 55.6	0.047[a]	–
B7 LSB	331.6	1875.0	1.77	0.171	0.220	− 25.0	0.11[a]	–
B7 USB	343.0	3750.0	1.71	0.175	0.203	− 26.8	0.090[a]	2 SpW of 1875 MHz

Note. [a]RMS of the aggregated bandwidth image.

of ^{13}CO and C^{18}O. We find that ^{13}CO is optically thick with $\tau_{13} > 3$ (at the v_{LSR}) everywhere that the line is significantly detected. The fifth column in Table 3 shows the median optical depth at the source velocity (-33.5 km s^{-1}) of the optically thick lines. This median is taken from within an ellipse of size 1.2 arcsec × 0.9 arcsec (P.A. 60°) centred on the tadpole, roughly corresponding to the lowest contour in the C^{18}O J=3–2 panel of Fig. 2. We show maps of the spatially resolved optical depth at the v_{LSR} in Appendix D.

3.2 Molecular column density

We compute the column density of each observed transition from the following equation:

$$N_{tot} = \frac{4\pi \, Q(T_{ex}) e^{E_u/kT_{ex}} B_\nu(T_{ex})}{hcg_u A_{ul}[J_\nu(T_{ex}) - J_\nu(T_{cmb})]}$$
$$\times \int T_{mb} \frac{\tau_v}{1 - e^{-\tau_v}} dv \ cm^{-2}, \qquad (2)$$

where $Q(T_{ex})$ is the rotational partition function for a given excitation temperature (the statistical sum over all rotational energy levels), g_u is the rotational degeneracy of the upper level with energy E_u, A_{ul} is the Einstein A coefficient for the transition, k is the Boltzmann constant, h is the Planck constant, B_ν is the Planck function, $J_\nu = (h\nu/k)/[\exp(h\nu/kT) - 1]$ is the Planck function in temperature units (K), and $\tau_v/(1 - e^{-\tau_v})$ is a correction factor for non-zero optical depth (see e.g. Goldsmith & Langer 1999). We obtain the relevant parameters for each molecule (frequency, rotational partition function, Einstein A coefficients, etc.) from the JPL Spectral Line Catalog (Pickett et al. 1998) and the Leiden Atomic and Molecular Database (Schöier et al. 2005). We report median column densities (using the same extraction region as for the optical depth) in Table 3. Maps of the spatially resolved column density calculation for each of the CO isotopologues are shown in Appendix F.

To compute the column density, we assume an excitation temperature of $T_{ex} = 20$ K. Assuming a single excitation temperature is a large source of uncertainty as this is often a poor assumption (see discussion in Mangum & Shirley 2015). The tadpole is embedded in the brightest portion of the H II region where temperatures are estimated to be somewhat higher ($\gtrsim$30 K; see e.g. Roccatagliata et al. 2013). At the same time, our data suggest that gas in the centre

of the tadpole remains cold (see Sections 3.4 and 3.6). Adopting a higher excitation temperature ($T_{ex} \approx 40$–80 K) or a variable excitation temperature, as described in Section 3.4, changes our results by a factor of $\lesssim$2 (see Appendix F and Fig. F1).

3.3 Molecular gas mass

We estimate the molecular mass of the tadpole from the C^{18}O as this is the least optically thick of the CO isotopologues. We compute the mass as follows:

$$M_{gas} = N(C^{18}O) \left[\frac{H_2}{C^{18}O} \right] \mu_g m(H_2) \pi a_{min} a_{max}, \qquad (3)$$

where [H$_2$/C^{18}O] = 4.85×10^6 is the abundance of H$_2$ compared to C^{18}O, $\mu_g = 1.36$ is the mean molecular weight, $m(H_2)$ is the mass of molecular hydrogen, and $a_{min} \approx 0.9$ arcsec and $a_{max} \approx 1.2$ arcsec are the minor and major axes of the tadpole, respectively. This gives a gas mass of ~0.6 M$_\odot$.

We use the C^{18}O column density to estimate the mass since both ^{12}CO and ^{13}CO are optically thick. However, in regions bathed in ionizing radiation, isotope-selective photodissociation may alter the relative abundance of optically thin isotopologues like C^{18}O (e.g. Keene et al. 1998). If isotope-selective photodissociation has reduced the abundance of C^{18}O, then this mass estimate will be a lower limit. This will also be the case if C^{18}O is optically thick.

We also estimate the mass of the small globulette located just below the tadpole tail (see Figs 1 and 5). We compute the globulette mass using the optically thin ^{12}CO emission (the globulette is not detected in C^{18}O). Using the abundance of H$_2$ compared to ^{12}CO, [H$_2$/^{12}CO] = 10^4 and again assuming $T_{ex} = 20$ K, we estimate a mass $M_{globulette} \approx 0.04 \, M_{Jupiter}$. This is a factor of a few smaller than the typical globulette mass in the Grenman & Gahm (2014) catalogue (this object is not in that sample).

3.4 CO emission towards the externally heated tadpole

We detect CO emission throughout the tadpole and measure high optical depths (see Table 3) that suggest that none of the isotopologues probe gas in the immediate environs of the HH 900 YSO (see Fig. 2). For the tadpole, the different appearance between the continuum (see Section 3.6) and the CO integrated lines (compare Figs 2 and 8) can be explained mostly by differences in optical depth.
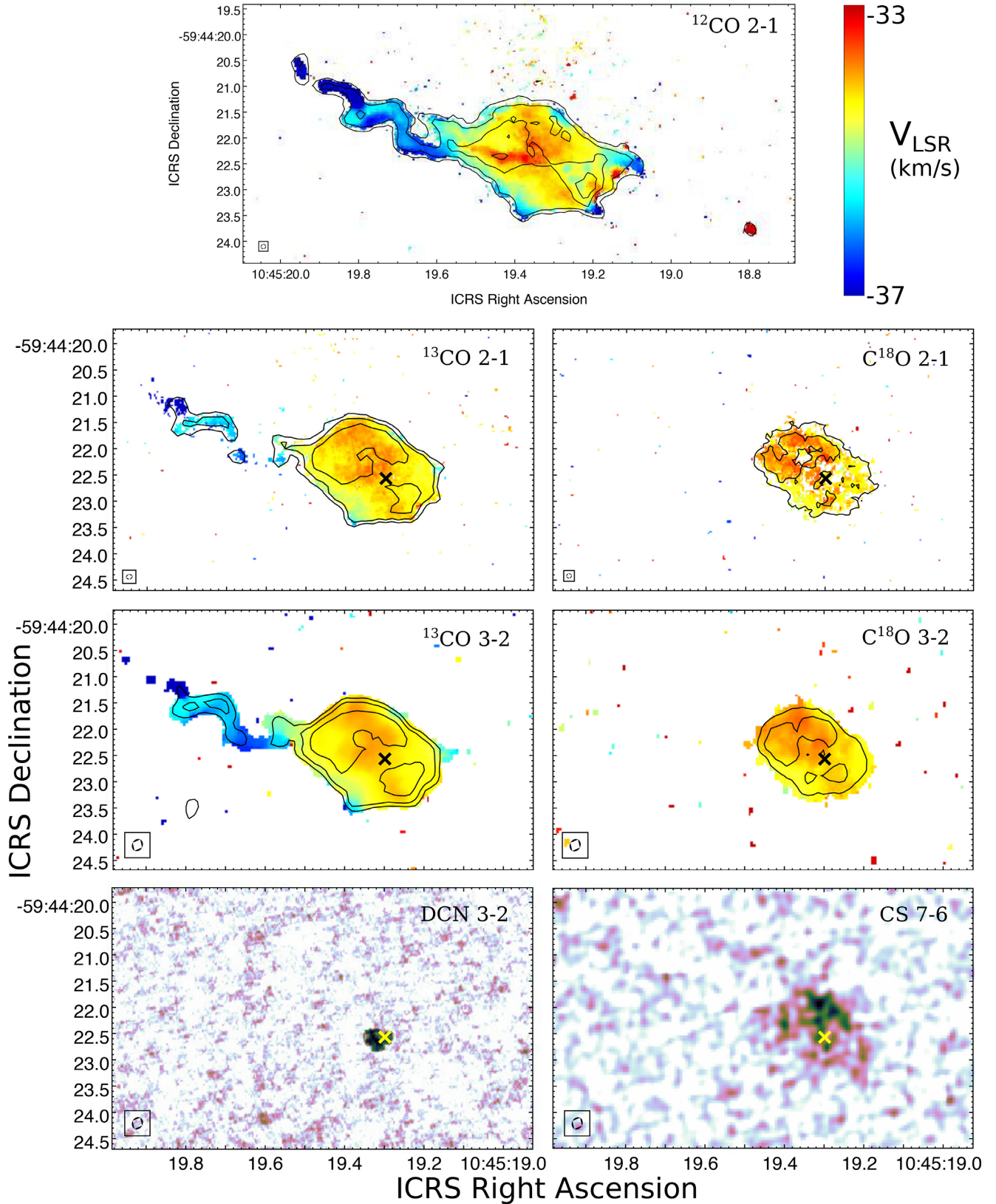
Figure 2. CO isotopologues panels show moment one maps with moment 0 contours overplotted. Contours of top panel are the same as in Fig. 1. For the other CO isotopologue panels, contour levels are -2 (dashed), 1, 2, 4, 8, and $16 \times \sigma$, with σ equal to 5.6 and 50 mJy km s^{-1} for ^{13}CO $J=2–1$ and $J=3–2$ and 5.4 and 42 mJy km s^{-1} for C^{18}O $J=2–1$ and $J=3–2$, respectively. The left and right bottom panels use a different colour scale and show the moment 0 of DCN $J=3–2$ and CS $J=7–6$ lines, respectively.

Table 3. Summary of molecular line derived physical properties. Columns are the species/transition, peak and median intensities, median column density if optically thin, median optical depth, and median column if optically thick, respectively.

Element	I_{peak} (K km s^{-1})	I_{median} (K km s^{-1})	$\log(N_{thin})_{median}$ (cm^{-2})	τ^a_{median}	$\log(N_{thick})_{peak}$ (cm^{-2})	$\log(N_{thick})_{median}$ (cm^{-2})
^{12}CO J=2–1	158.6	69.3	16.5	209	20.7	19.0
^{13}CO J=2–1	75.1	33.5	16.2	6.0	18.4	17.1
C^{18}O J=2–1	61.7	24.0	16.1	–	–	–
DCN J=3–2	16.9	3.1	13.1	–	–	–
^{13}CO J=3–2	67.5	40.6	16.3	4.7	18.1	17.1
C^{18}O J=3–2	31.6	15.5	15.9	–	–	–
CS J=7–6	13.7	7.3	13.6	–	–	–

Note. ^{a}Median value taken at the source velocity, $v_{LSR} = -33.5$ km s^{-1}.
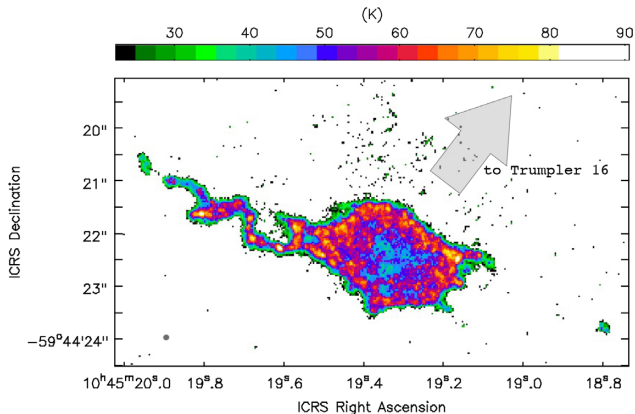
Figure 3. Peak brightness temperature of ^{12}CO J=2–1.

Assuming [H$_2$/CO]=10^4 and a linewidth of 1 km s^{-1}, the ratio between the peak optical depth of the CO J=2–1 line and that of dust is approximately 10^5. This means that a tadpole mass $\gtrsim 0.01$ M$_\odot$ is sufficient to ensure optically thick CO conditions. Therefore, we can use the Eddington–Barbier approximation and assume that Fig. 3 is showing the temperature of the tadpole at different depths. Because lines of sight directed farther from the centre of the tadpole probe layers located at larger radii, the limb brightening shown in Fig. 3 is interpreted as a positive radial ($\frac{dT}{dr} > 0$) temperature gradient (external heating). This gradient seems to characterize the tadpole at least as deep as the CO line can probe.

Limb brightening is the main evidence for a positive radial temperature gradient. In this spatially resolved source, lines of sight closest to the globule edge trace primarily surface material where we measure a larger brightness temperature. Two additional lines of evidence support this interpretation.

Less abundant isotopologues like ^{13}CO and C^{18}O can trace deeper, and therefore, probe colder material in the tadpole than ^{12}CO. Assuming optically thick emission, this means that the $\tau = 1$ surface will be deeper in the globule for rarer isotopologues. If this is the case, the observation that $T_b(^{12}\text{CO}) > T_b(^{13}\text{CO}) > T_b(\text{C}^{18}\text{O})$ (see Appendix E and the peak brightness temperature maps in Fig. E1) indicates a thermal gradient. We compute high optical depths for both ^{12}CO and ^{13}CO (see Section 3.1). We do not have the data to constrain the optical depth of the C^{18}O, although it may be optically thin along lines of sight away from the HH 900 YSO. We note that higher brightness temperatures from more abundant species are also expected under optically thin conditions.

The J=2–1 to 3–2 line ratios also suggest that all three isotopologues are optically thick. We show the median intensity of each CO isotopologue towards the HH 900 YSO in Fig. 4. The median is taken within a circle of radius 0″.3 centred on the position listed in Table 5. The peak temperatures of ^{13}CO and C^{18}O are similar for both the J=2–1 and 3–2 transitions. This is expected for optically thick lines as $T_{mb} \approx T_{ex}$ when $\tau \gg 1$ (the opacities for both transitions are within a factor of 2 for 8 K$<T_{ex}<$100 K). Optically thin emission at $T_{ex} \sim 16$ K would also predict similar peaks for the J=2–1 and 3–2 lines in local thermodynamic equilibrium (LTE). However, $T_b(^{13}\text{CO}) > 16$ K, indicating optically thick emission.

One additional notable feature of the CO lines is that, despite their high optical depth, their shapes do not show the self-absorbed profiles usually observed in CO towards star formation regions. Indeed, towards the tadpole, the profiles shown in Fig. 4 display a single peak and are roughly symmetric, reminiscent of optically thin lines.

Line emission from a cloud with a temperature gradient is characterized by different parts of the line tracing material with different excitation temperatures. At the line peak, where line opacity is highest, the emission is tracing on average more external layers of the core compared with emission at velocities in the sloping wings of the line. The specifics of the thermal gradient depend on the incident radiation and the density profile of the cloud. Nevertheless, a positive radial thermal profile can explain the lack of self-absorption: Intervening material in outer layers is warmer, so it does not decrease the intensity of lines arising from colder inner regions.

3.5 The molecular outflow associated with the irradiated HH 900 jet+outflow system

We report the first detection of the cold, molecular outflow associated with the HH 900 jet+outflow system (see Figs 5 and 6). Two biconical outflow cavities (opening angles of ∼50°) emerge from the protostar detected in the globule (discussed in the next Section). The lobes are redshifted and blueshifted in the same sense as the irradiated jet+outflow components seen outside the globule (see Fig. 7). The biconical cavities open to the same width as the globule at the edge. Structure in the blueshifted ^{12}CO J=2–1 emission traces the uneven edge of the globule, protruding beyond the boundaries of the globule delineated by the optically thin isotopologues (see Fig. 5). These extensions from the outflow cone overlap with two of the three small dust streamers seen in silhouette in the *HST* images (see Fig. 1). Smith et al. (2010) suggested that these streamers are limb darkened by dust in the side walls of the outflow cavity. A third streamer, located closer to the major axis of the globule (see Fig. 1), is also seen in CO but it does not appear to be blueshifted (see Fig. 5). In this environment, the molecular outflow is only detected
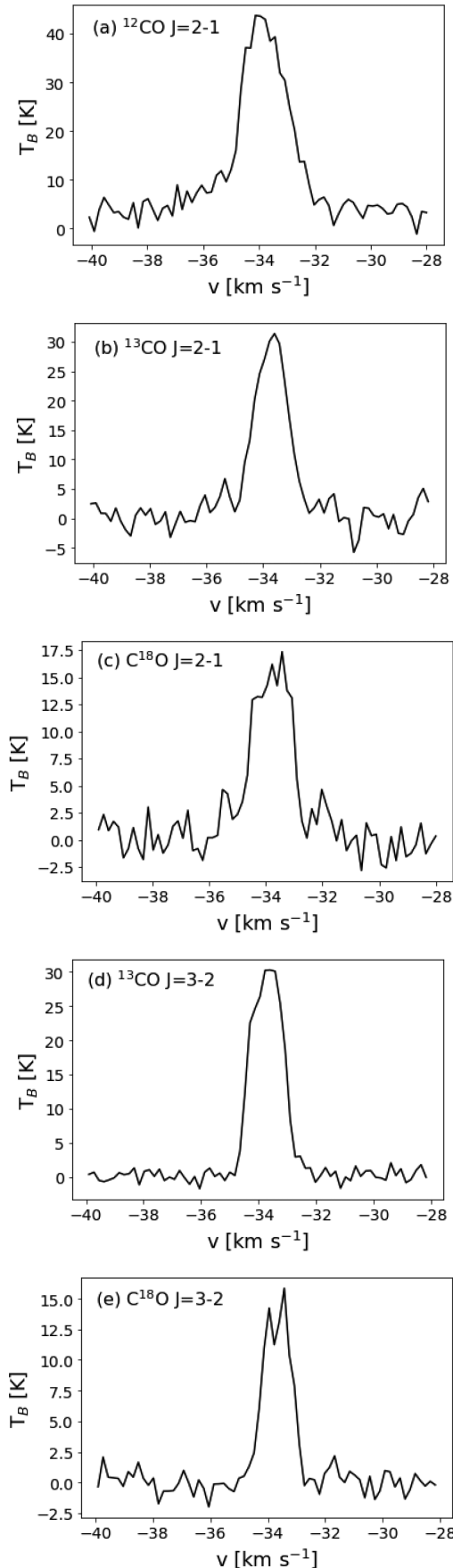
Figure 4. Median CO line profiles near the HH 900 YSO. Panels (a)–(e) display the molecule and transition in their top left corner.

within the protection of the high-density globule. The outflow is not seen in either transition of ^{13}CO or $C^{18}O$.

To estimate the physical parameters of the outflowing gas, we integrate the line emission in regions enclosed within the lowest contour in Fig. 5 (as described in the figure caption, these are 26.4 K km s^{-1} for the red lobe and 25.9 K km s^{-1} for the blue lobe). In the blueshifted case, we integrate only inside the roughly conical/triangular shape extending to the south-west from the continuum source. Fig. 6 shows the average ^{12}CO and ^{13}CO J=2–1 emission from these two regions. Redshifted wing emission is prominent, extending up to +19 km s^{-1} from the globule's v_{LSR} ($v_0 = -33.5$ km s^{-1}). The blueshifted side displays evident wing emission starting from ($v_0 - 3.5$) km s^{-1} up to radial velocities of ($v_0 - 24$) km s^{-1}.

To evaluate mass, momentum, and energy contained in the outflow lobes, we use the velocity moments of the CO J=2–1 line following the methods described in Calvet, Canto & Rodriguez (1983). We directly integrate the profile in the line wings – $|v - v_0| > 3.5$ km s^{-1} – and correct for the low-velocity outflow material following Margulis & Lada (1985). We assume optically thin conditions for the high-velocity wing emission, a single excitation temperature $T_{ex} = 100$ K, and an [H$_2$/CO] abundance ratio of 10^4. The adopted excitation temperature is consistent with that found towards outflow gas in low- and intermediate-mass stars (van Kempen et al. 2009; Guzmán et al. 2011; Yıldız et al. 2012; Gómez-Ruiz et al. 2019). As shown in Fig. 6, ^{13}CO is not detected in the wings, consistent with CO opacities $\leq$0.1 in the outflow. The obtained physical parameters, uncorrected for inclination, are given in Table 4.

Reiter et al. (2015b) estimated that the jet is tilted $\lesssim$10° from the plane of the sky (corresponding to an inclination angle of $i \gtrsim 80°$, where $i = 90°$ lies in the plane of the sky). Assuming that all outflowing material is directed along the outflow axis, the inclination corrections for the momentum, energy, mass-loss rate, and momentum rate are $(\cos i)^{-1}$, $(\cos i)^{-2}$, $\tan i$, and $(\cos i)^{-2}\sin i$, respectively, where i is the inclination angle between the outflow axis and the line of sight. However, we caution that a large fraction of the material in molecular outflows moves in directions transverse to the outflow axis, thus making these naive inclination corrections lead to an overestimate of the outflow parameters when compared to simulations (Downes & Cabrit 2007). Furthermore, considering that the semi-opening angle of the outflow is 27.5° and that there is no discernible blue- or redshifted emission associated with the opposite lobe, following Cabrit & Bertout (1986) we conclude that $i \leq 62.5°$. This is somewhat less than the $i \gtrsim 80°$ estimated in Reiter et al. (2015b). Uncertainties in the velocities, and therefore inclination estimates, determined from optical spectroscopy are large as they are measured much less precisely than those from millimetre emission lines. Accounting for an uncertainty of ~5° (from the optical), the inclination estimates remain discrepant, leaving open the possibility that the jet and the molecular outflow have different inclination angles.

Using $T_{ex} = 50$ K decreases the mass estimate by ~40 per cent. The uncertainties include those derived from the noise of the data and the flux scaling, but they do not reflect the systematic uncertainties such as distance, inclination, abundance variations, or fraction of outflow material confused within the local v_{LSR}.

Our spectral set-up included SiO J=5–4 that has been observed to trace the collimated, high-velocity jet in some cases (e.g. Codella et al. 2007; Codella et al. 2013; Leurini et al. 2013). However, this line is not detected anywhere in our ALMA map. We note that the upper energy level of SiO J=5–4 is a factor of ~2 higher than ^{12}CO,
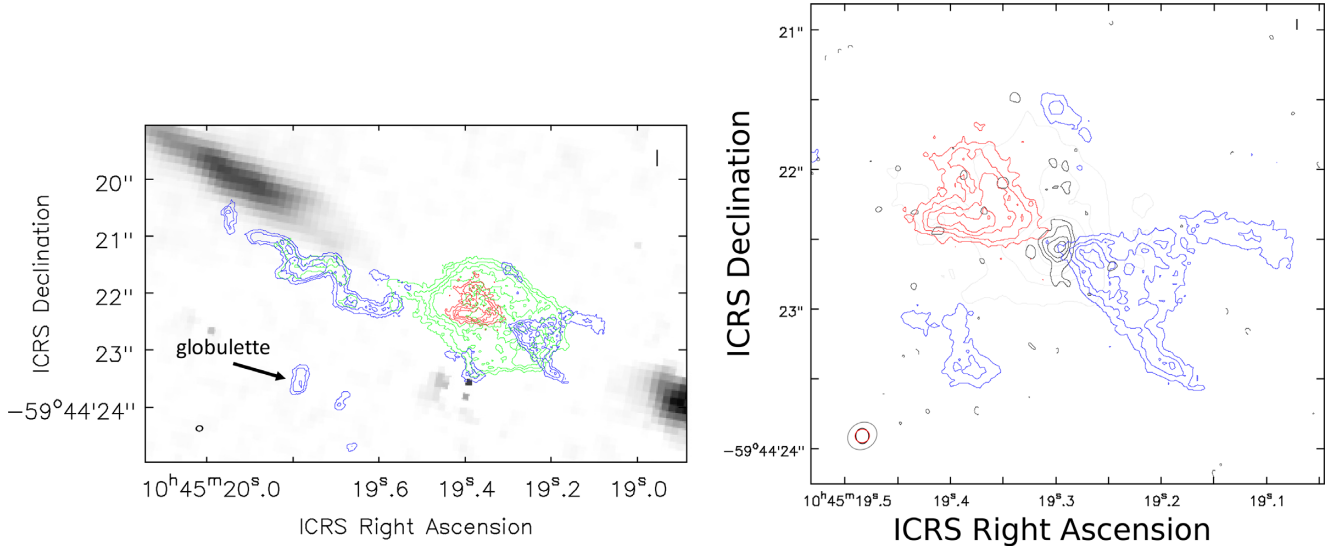
Figure 5. Red and blue contours in both the panels show the integrated emission from the wings of the CO J=2–1 line (using [−57, −37] and [− 30, −11] km s^{-1} for the blue and red lobes, respectively). Beams are shown in the lower left corner of each panel. Dashed contours mark negative levels. Contour levels: blue: −3, 7, 13, 19, and 25 × σ = 3.7 K km s^{-1}; red: −3, 8, 16, 24, and 32 × σ = 3.3 K km s^{-1}. *Left:* Grey-scale: [Fe II] emission from *HST* as shown in Reiter et al. (2015b). Green contours show the integrated ^{13}CO J=2–1 line. Levels: −3, 15, 30, 45, and 60 × σ = 1 K km s^{-1}. *Right:* Zoom in into the outflow region. Black and grey contours show the continuum emission at 232.2 GHz imaged using robust weighting parameters −0.5 and 1.0, respectively. Black levels: −3, 3, 5, 7, and 10 × σ = 108 μJy beam^{-1}; grey levels: −5, 5, 10, 15, 25, and 40 × σ = 52 μJy beam^{-1}.
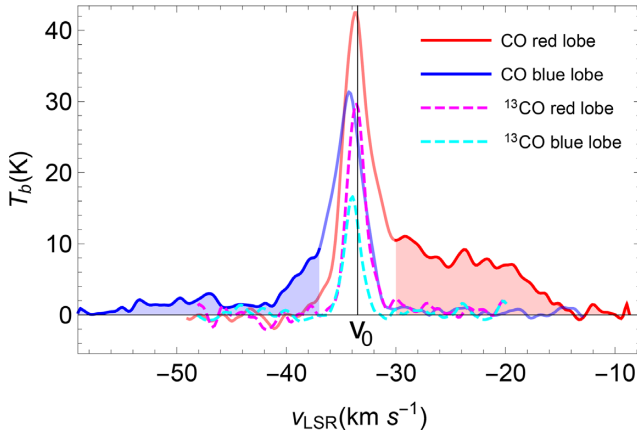
Figure 6. Profiles of the average CO and ^{13}CO J=2–1 emission within the red- and blueshifted lobes of the biconical outflow detected towards the HH 900 YSO. A vertical line marks the assumed central v_{LSR} of −33.5 km s^{-1}. Shaded regions indicate the blue- and redshifted wing emission extending between [−57, −37] and [− 30, −11] km s^{-1}, respectively.

leaving open the possibility that lower J transitions of SiO may be detectable. However, the lack of SiO emission is consistent with the relatively low outflow velocity. Gas phase SiO is thought to be produced when Si is removed from grains by either sputtering or grain–grain collisions. To produce the observed column densities of SiO in molecular outflow regions requires shock velocities of ≈25 km s^{-1} and densities of the order of 10^5 cm^{-3} for sputtering (Schilke et al. 1997; Gusdorf et al. 2008) or grain–grain collisions (Caselli, Hartquist & Havnes 1997).

Combining the outflow length, R_{lobe}, and velocity yields the dynamical age, $t_{dyn} = R_{lobe}/v$. We use the dynamical age to calculate the outflow mass-loss rate, $\dot{M}_{out} = M_{out}/t_{dyn}$. To estimate the momentum of a jet-driven molecular outflow, we follow prescriptions of Downes & Cabrit (2007) and use the quantities in

Table 4 without any inclination correction. Note also that from Fig. 6 both redshifted outflowing material in the blueshifted outflow lobe and vice versa are either negligible or they appear entirely confused with the material at v_0. For the force, we follow their 'perpendicular' method with $R_{lobe} = 0.''6 \times d = 1380$ au for both lobes. Using the velocities in Table 4, we get

$$\dot{P}_{blue} = \frac{1}{3}\frac{P_{blue}}{|R_{lobe}/(v_{blue} - v_0)|} = -6.5 \times 10^{-5}~M_\odot~\text{km s}^{-1}~\text{yr}^{-1}~,$$

$$\dot{P}_{red} = \frac{1}{3}\frac{P_{red}}{|R_{lobe}/(v_{red} - v_0)|} = 8.5 \times 10^{-5}~M_\odot~\text{km s}^{-1}~\text{yr}^{-1}~.$$

3.6 Dust continuum emission

We detect two point-like sources in each of the continuum bands observed. Fig. 8 shows the two point sources; the first resides inside the tadpole globule, on the jet axis and at the origin of the molecular outflow (see Section 3.5). We propose that this source is the YSO that drives the HH 900 jet+outflow system (the HH 900 YSO), seen for the first time with ALMA (Fig. 5). The second continuum source coincides with the YSO that lies in the western limb of the HH 900 outflow. Povich et al. (2011) identified this object as a candidate YSO, PCYC 838, based on model fits to the IR spectral energy distribution (SED; see Fig. 1 and Appendix C). A third star, just beneath the southern edge of the tadpole globule, is not detected with ALMA (PCYC 842; see Fig. 1).

Fig. 8 shows that most of the continuum emission from the tadpole comes from the compact source whose central position is given in Table 5. This source, the HH 900 YSO, is slightly offset (0.''5) from the centre of the tadpole's head, which forms an extended envelope around it. The tadpole's head is most evident in the CO lines and visible as faint extended emission in the Band 6 images (with highest sensitivity).

Table 5 gives the flux densities arising from a region within a radius of 0.''3 (corresponding to $r_0 = 690$ au at the distance to Carina) from the HH 900 YSO as well as the spectral index of a power-law fit
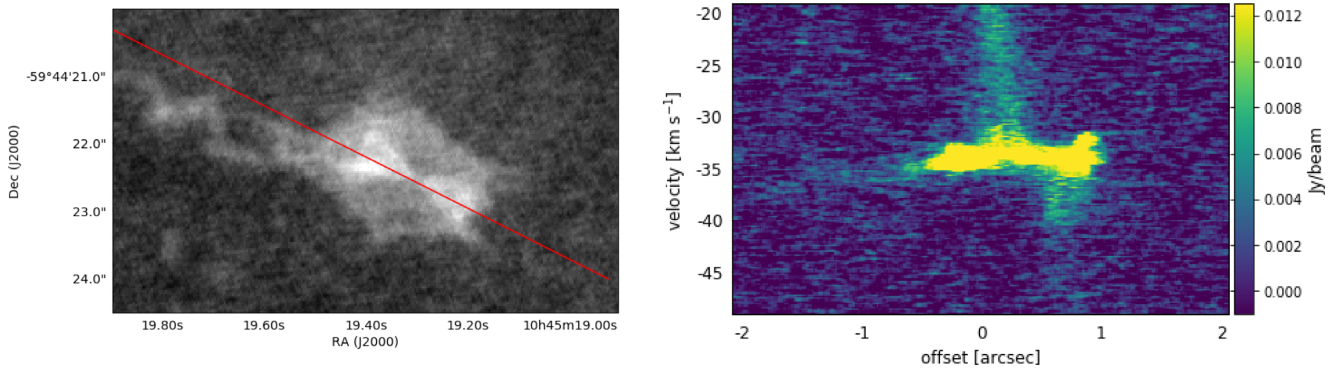
Figure 7. Tracing location (*left*) used to make the position–velocity diagram (*right*) of the ^{12}CO $J=2$–1 showing the molecular outflow associated with HH 900. Emission is summed in a $0\rlap{.}''25$ aperture.

Table 4. Summary of the physical properties of the outflow. For the red and blue lobes of the outflow, columns are the mass of outflow, velocity, momentum, kinetic energy, length of the lobe, dynamical time, mass-loss rate, and momentum flux.

Lobe	M_{out} (10^{-3} M$_\odot$)	$v - v_0$ (km s^{-1})	P (10^{-2} M$_\odot$ km s^{-1})	K.E. (10^{40} erg)	R_{lobe} (pc)	t_{dyn} (yr)	$\dot{M}_{out}$ (M$_\odot$ yr^{-1})	$\dot{P}$ (M$_\odot$ yr^{-1} km s^{-1})
Blue	3.36 ± 0.5	-6.45	-2.17 ± 0.3	260 ± 70	0.007	1060	3.2×10^{-6}	-6.5×10^{-5}
Red	3.15 ± 0.5	7.96	2.51 ± 0.3	280 ± 70	0.007	860	3.7×10^{-6}	8.5×10^{-5}

Note. Using $T_{ex} = 100$ K. Quantities are not corrected for inclination or opacity.
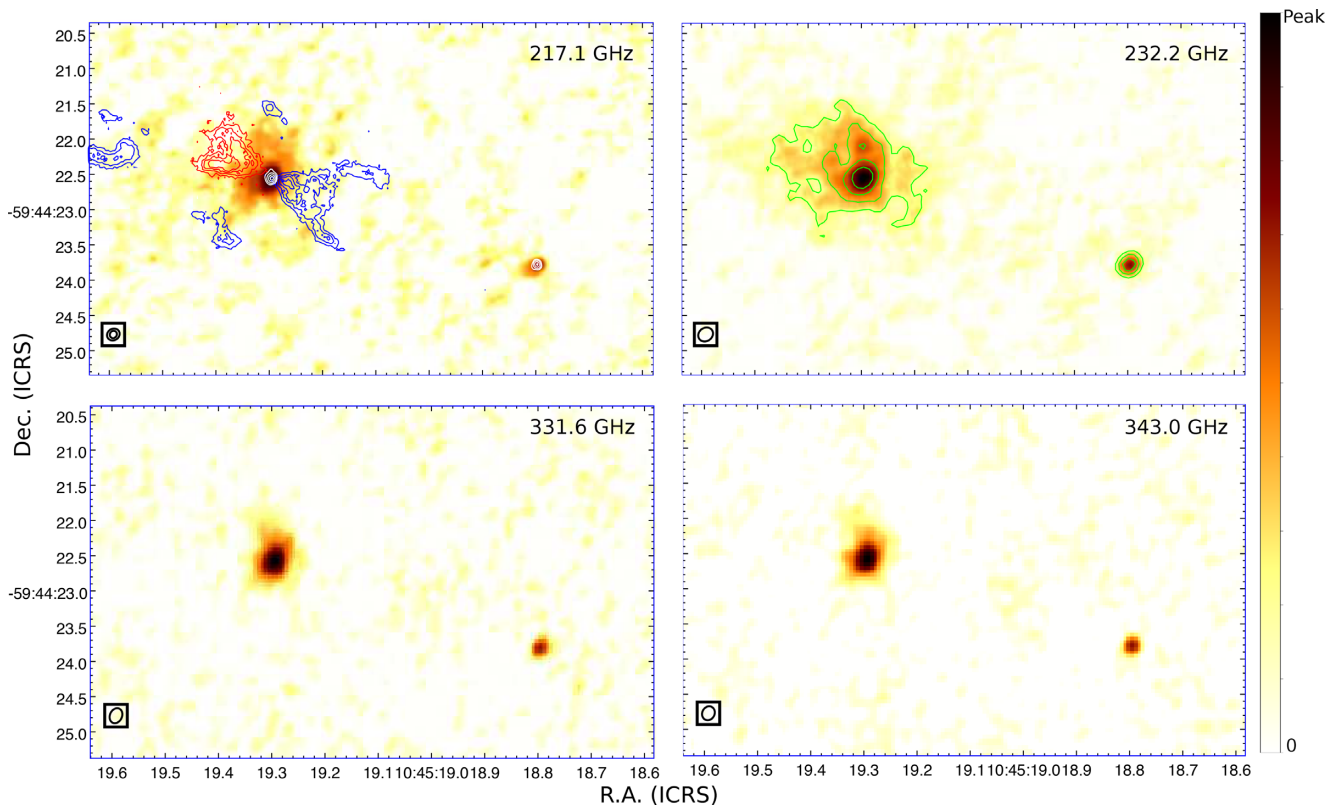
Figure 8. Continuum emission at the four frequencies listed in Table 5. Beams are indicated in the bottom-left corner of each panel. *Top left panel.* Peak: 1.58 mJy. White contours at 4, 6, 9, 12, and 15 $\times \sigma = 0.82$ mJy beam^{-1} show the 232.2 GHz continuum imaged using only long (>400 kλ) baselines. We also display the same red and blue contour levels from CO $J=2$–1 wing emission as in Fig. 5. *Top right panel.* Peak: 2.43 mJy beam^{-1}. The five green contours levels are linearly spaced between 4 $\times \sigma = 0.47$ mJy beam^{-1} and the peak. *Bottom left panel.* Peak: 5.32 mJy beam^{-1}. *Bottom right panel.* Peak: 5.68 mJy beam^{-1}.

Table 5. Position and flux densities from the compact continuum source.

Source	R.A. (J2000)	Decl. (J2000)	217.1 GHz (mJy)	232.2 GHz (mJy)	331.6 GHz (mJy)	343.0 GHz (mJy)	α^a
HH 900 YSO[b]	10:45:19.296	−59:44:22.55	4.70	5.86	12.54	13.48	2.2 ± 0.5
Tadpole head	–	–	25.2	38.7	16.8	14.9	–

Notes. [a]Spectral index of best power-law fit to flux densities ($S_\nu \propto \nu^\alpha$).
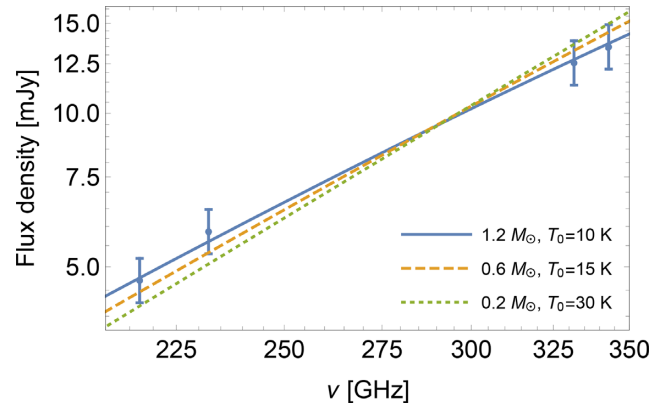[b]Within a radius of $0\overset{''}{.}3$ from peak.

to these fluxes. We obtain the best-fitting model by minimizing the squared differences between the model and the fluxes, weighted by the inverse of their squared uncertainties. Assuming flux densities have an uncertainty of 15 per cent, we derive 1σ error bars in the spectral index of ± 0.5 (following, e.g. Lampton, Margon & Bowyer 1976). These error bars are due in part to the frequency span of our observations, with adjacent bands (6 and 7) not being optimal to estimate accurate spectral indices.

Nevertheless, the derived spectral indices are lower than those expected from optically thin thermal dust emission in the Rayleigh–Jeans limit – given by $\beta + 2$ – assuming that the dust absorption coefficient behaves as $\kappa_\nu = \kappa_0 (\nu/\nu_0)^\beta$. Because the brightness temperature of our highest resolution continuum images peaks at about ∼4-5 K, it is not likely that the fluxes are dominated by optically thick dust emission. Therefore, the remaining option to explain the flat spectrum must be a combination of low temperatures (making Rayleigh–Jeans less applicable) and low β. Relatively flat mm SEDs are not uncommon in dense regions of star formation (e.g. Guzmán et al. 2014; Orozco-Aguilera et al. 2017), and they are usually attributed to a β parameter lower than that of the diffuse ISM dust (characterized by $\beta \gtrsim 1.5$) due to dust coagulation (Draine 2006).

We model the fluxes towards the HH 900 YSO as arising from a spherical dusty core with a density profile $\rho \propto r^{-2}$, representing the outer envelope of an accreting young star (McKee & Ostriker 2007). We assume a dust absorption coefficient as described above with $\nu_0 = 230.61$ GHz (1.3 mm), $\kappa_0 = 0.8$ cm^2 g^{-1} (Ossenkopf & Henning 1994), a $\beta = 1.0$, and a gas-to-dust mass ratio of 100. We assume a temperature profile $T(r) = T_0 * (r/r_0)^{-0.4}$, where $r_0 = 690$ au. We expect this radially decreasing temperature gradient near the HH 900 YSO [this model is for emission within a radius of 690 au ($0\overset{''}{.}3$) of the YSO], although this gradient reverses on larger scales due to the external influence of environment (see Section 3.4 and Paper I). This profile is characteristic of an optically thin, centrally illuminated dusty core with $\beta = 1.0$ (Adams & Shu 1985).

Fig. 9 shows best-fitting models and derived masses of the core assuming different T_0 values. For comparison, using a homogeneous temperature of 15 K and the formula $M = S_\nu d^2/B_\nu(T)\kappa_\nu$ we obtain 1.0 M$_\odot$ for the compact HH 900 YSO core. Given the limited sampling of the continuum SED, we do not attempt to fit a (poorly constrained) blackbody to estimate the luminosity and therefore infer a mass of the HH 900 YSO. For a young jet-driving source, we expect the SED to peak at wavelengths shorter than we have observed with ALMA. Unfortunately, the HH 900 YSO is confused with the two other protostars near the globule in existing data (from 70 to 500 μm with, e.g. *Herschel*; see Ohlendorf et al. 2012).

To compute the mass of the entire globule, we use only the Band 6 continuum emission. The size of the tadpole head is a significant fraction of the size of the MRS of the Band 7 images (see Table 1), making it difficult to recover extended, low-surface-brightness emission accurately during deconvolution. All reported fluxes are likely lower bounds (see discussion in Appendix B and

Figure 9. Spectral energy distribution and dust emission models adjusted to the fluxes measured towards HH 900 YSO within a radius of $0\overset{''}{.}3$ from the peak continuum position (Table 5).

Fig. B1). We adopt a higher temperature for the extended emission around the compact source (45 K; see Section 3.4) to compute a mass of 1.9 M$_\odot$ for the entire tadpole. If we instead assume 15 K, as for the compact source, the estimated tadpole mass is 7.3 M$_\odot$. We make the conservative choice to adopt a mass of 1.9 M$_\odot$ for the remainder of our analysis, although this is likely to be a lower bound.

3.7 Extended emission near the HH 900 YSO

Continuum emission from the HH 900 driving source appears to be marginally resolved at 217 and 232 GHz. The major axis extends perpendicular to the jet axis. We estimate an inclination angle of $i \lesssim 62.5°$ (see Section 3.5) for the HH 900 outflow. With this orientation, the circumstellar disc around the HH 900 jet-driving source should be viewed nearly edge-on.

Emission lines targeted in this study have been used to measure the size and kinematics of gas discs around low-mass stars (e.g. Andrews et al. 2012; Tobin et al. 2012, 2015; Ansdell et al. 2018). Despite the favourable orientation, the CO lines are too optically thick to probe the kinematic structure in the circumstellar material. A higher excitation tracer like CH$_3$CN (e.g. Oya et al. 2016) may provide more information on the kinematics of the gas closest to the protostar.

We also report the serendipitous detection of DCN J=3–2 (see Table 3). Fig. 10 shows the integrated emission towards the tadpole. DCN is observed near the location of the protostar, but it forms an asymmetric envelope that seems to wrap the HH 900 YSO from the south. DCN is usually detected in cold gas (e.g. Caselli & Ceccarelli 2012). In their study of high-mass star-forming regions, Gerner et al. (2015) find a higher fraction of deuterated molecules (including DCN) in colder, less luminous regions. At low temperatures ($\lesssim$10 K) and high densities ($\gtrsim 3 \times 10^4$ cm^{-3}; see e.g. Bacmann et al. 2002), CO freezes out of the gas phase, enabling deuterium fractionation
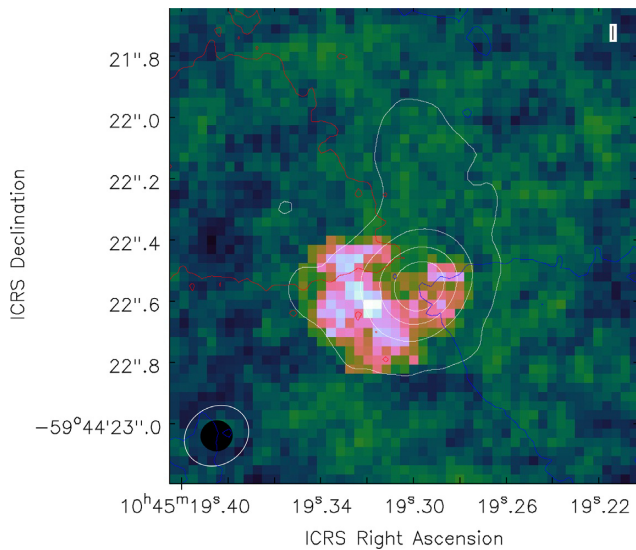
Figure 10. Integrated DCN emission towards the tadpole. Peak: 16.9 K km s^{-1}. White contours show the 232.2 GHz continuum emission. Red and blue outflow contours show the first positive level displayed in Fig. 5.

(Bergin & Tafalla 2007). While we do not have a direct measure of the gas temperature near the protostar, we take the detection of DCN as evidence that the gas is cold, creating favourable conditions for the formation of DCN. DCN is typically detected towards regions of H_2 column density (as estimated from the continuum) of $\gtrsim 3 \times 23$ cm^{-2}. The typical abundance of HCN ranges between 1×10^{-7} and 1×10^{-9} (Roberts et al. 2002). In the absence of fractionation, [DCN/HCN]$\sim 1 \times 10^{-5}$, implying a column density of DCN $< 1 \times 10^{12}$ cm^{-2}, associated with a line peak <1 K. We observe 15 K and estimate a DCN column density of $\gtrsim 1 \times 10^{13}$ cm^{-2} (see Table 3). This is typical: The detection of the deuterated species guarantees some fractionation.

3.8 Virial mass estimate

We estimate the virial mass of the tadpole globule as a whole assuming that it is a self-gravitating sphere. We compute the virial mass using the following expression:

$$M_{\text{vir}} = \frac{3(5-2n)}{8(3-n)\ln(2)} \frac{(\Delta V)^2 R}{G} \quad , \tag{4}$$

where n is the exponent of the density profile ($\rho \propto r^{-n}$), $\Delta V = 1.4$ km s^{-1} is the linewidth of C^{18}O J=2–1, $R = 3000$ au is the mean radius of the cloud, and G is the gravitational constant (see e.g. MacLaren, Richardson & Wolfendale 1988). Correction factors for non-spherical clouds change equation (4) by less than 10 per cent (Bertoldi & McKee 1992). We consider two density profiles for the globule. For a density profile that decreases with radius, $\rho \propto r^{-2}$, the estimated virial mass is $\sim$3.6 M$_\odot$. For a constant density profile, $\rho = constant$, this estimate increases to 6.0 M$_\odot$, similar to the mass (7.3 M$_\odot$) we derive assuming cold dust (T=15 K) in Section 3.6. As a gravitational mass, these estimates include the mass of the HH 900 YSO. Neither estimate includes the pressure of the external environment, although the physical parameters derived in Paper I suggest that this will be important. We leave a more complete exploration of the effect of the external environment to Paper III.

3.9 Cold gas kinematics

To examine the gas kinematics in the globule as a whole, we plot position–velocity (P–V) diagrams of emission parallel and perpendicular to the HH 900 outflow axis. Fig. 11 shows the slice locations and the P–V diagrams of ^{13}CO and C^{18}O J=3–2 emission. Both of the ^{13}CO P–V diagrams trace a C-shaped velocity structure with velocities near the globule centre that are $\gtrsim$1 km s^{-1} redder than those near the edges. Most of the C^{18}O emission in the parallel P–V diagram is close to the v_{LSR}, coinciding with the reddest velocities in the ^{13}CO P–V diagrams. In contrast, the C^{18}O in the perpendicular P–V diagram traces a similar C-shape to that seen in the ^{13}CO. We show a few vertical slices through the perpendicular P–V diagram in Fig. 11. Emission profiles from both isotopologues tend to be quite broad in velocity space, with a peak intensity at bluer velocities closer to the edge of the globule. We discuss possible interpretations of this shape in Section 5.2.

4 A PHOTOEVAPORATING JET+OUTFLOW SYSTEM

Reiter et al. (2015b) suggested that the HH 900 jet+outflow system is the irradiated analogue of jet-driven molecular outflows seen in more quiescent environments (e.g. HH 111; Lee et al. 2000; Lefloch et al. 2007). Fig. 12 shows a schematic of the HH 900 jet+outflow emerging from the tadpole. Only ionized gas tracers like H α trace the full extent of the outflow outside the globule. Hot molecular gas – H_2 – and partially ionized gas – [C I] – are detected in the irradiated outflow near the globule, but extend less than half the length of the irradiated outflow (see Reiter et al. 2015b, and Paper I, respectively). With ALMA, we detect the molecular outflow inside the tadpole globule for the first time. The wide-angle molecular outflow (opening angle $\sim$50°) has a conical morphology that reaches the same width as the globule at the edge. This coincides perfectly with the H α outflow that is as wide as the globule where it emerges, before gradually tapering to terminus of jet (see Fig. 5 and Paper I). The abrupt end of the molecular outflow at the globule edge suggests that molecules are rapidly destroyed outside the protection of the optically thick globule. This structure is consistent with diagnostics presented in Paper I that show an increase in the excitation in the outflow with increasing distance from the globule.

Multiwavelength observations of the HH 900 jet+outflow system show layers of emission with the fastest material along the jet axis surrounded by slower gas in wider angle components. This onion-like morphology and velocity structure has been seen in nearby outflow systems in less complicated environments (e.g. DG Tau; see Bacciotti et al. 2000; Pyo et al. 2003). Forbidden emission lines (e.g. [Fe II]) trace the highest density and most highly collimated portions of the jet. Molecular (H_2) and ionized (H α) gas in the irradiated outflow are wider angle, with the H α morphology coinciding with the jet ([Fe II]) only at the terminus of the continuous inner outflow (Reiter et al. 2015b). The cold molecular outflow (CO) has a biconical morphology, originating from the HH 900 YSO in the centre of the globule and opening to the same width as the H α and H_2 by the time it reaches the globule edge.

The velocities of each component are also consistent with an onion-like structure. The fastest material, with radial velocities of $\pm\sim$40 km s^{-1} traced by [Fe II], is confined to the highly collimated jet. The surrounding layers of wider angle gas are slower, reaching the same velocities as the fast jet only where the two components coincide at the terminus of the continuous inner outflow. The cold molecular gas traces the slowest material, with velocities roughly an
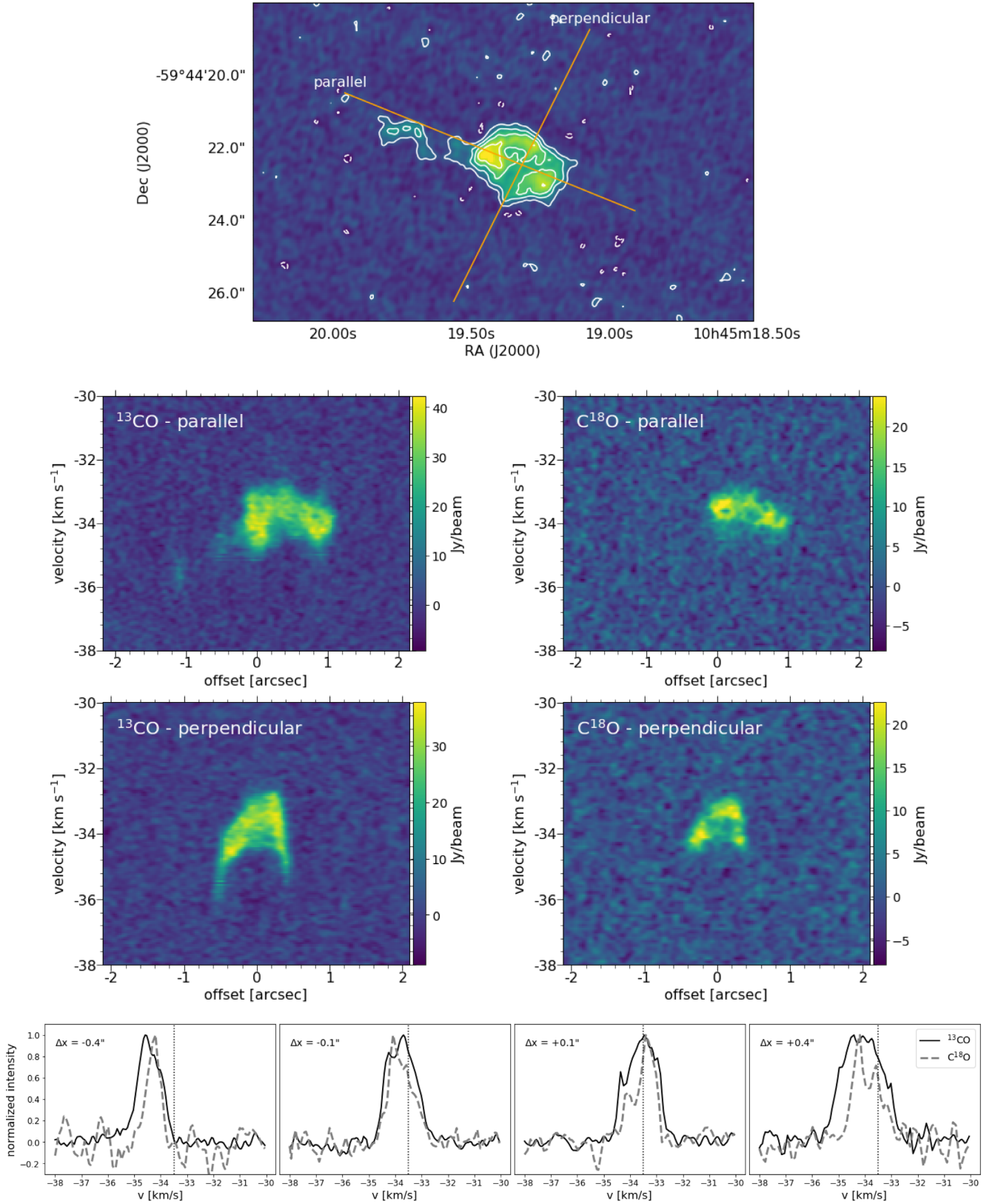
Figure 11. *Top:* Moment 0 map and contours showing the ^{13}CO J=3–2 emission with lines showing the slices made through the globule to produce the P–V diagrams shown below. Emission is summed in an aperture that is $0\rlap{.}''25$ wide. *Middle:* P–V diagrams of ^{13}CO and C^{18}O J=3–2 through the major axis of the globule, parallel to the outflow axis (*upper*) and perpendicular to the outflow axis (*lower*). *Bottom:* Emission profiles as a function of velocity for a few positions in the perpendicular P–V diagrams (these correspond to the sum of emission in five-pixel wide vertical slices through the P–V diagrams); ^{13}CO is shown with a solid black line, C^{18}O with a grey dashed line, and a dotted line indicates the $v_{\rm LSR}$.
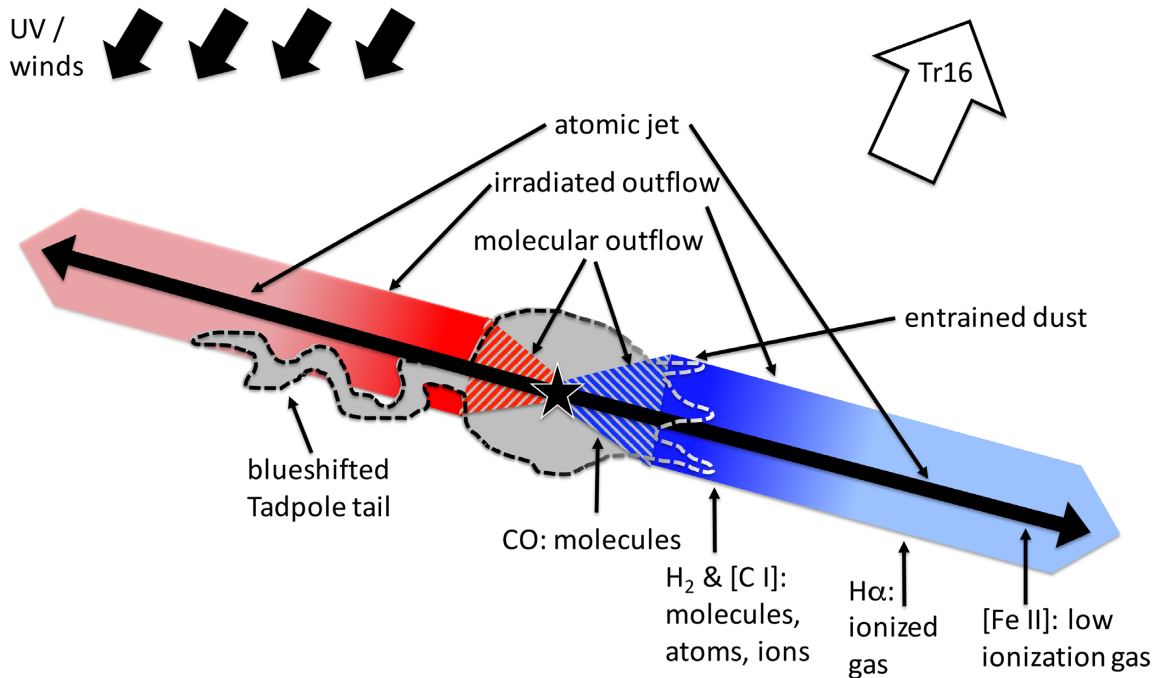
Figure 12. Cartoon rendering of the tadpole (grey) and the HH 900 jet+outflow system (red and blue). The *jet* (shown in black) is seen in low-ionization species that trace the predominantly neutral gas; the ionization state of the *outflow* transitions from mostly molecular inside the globule to mostly ionized as it propagates into the H II region (red and blue colour gradients). The tadpole tail is blueshifted in front of the redshifted side of the outflow and is physically distinct from the outflow.

order of magnitude slower than the jet-like components of HH 900 (see Section 3.5).

Various models propose that molecular outflows result from jet entrainment (e.g. Raga & Cabrit 1993; Lee et al. 2000; Arce & Goodman 2001; Ostriker et al. 2001) or represent a separate component altogether that is launched at slower velocities from larger radii in the disc (e.g. Pudritz & Norman 1986; Ferreira 1997). The tapering of H α emission with increasing distance from the tadpole is difficult to explain as there is no obvious physical mechanism that could recollimate the ionized outflow. However, the swept-up shell of a jet-driven molecular outflow will naturally have this morphology (see fig. 2 in Arce et al. 2007) and a Hubble-flow like velocity structure, as seen in H α (Reiter et al. 2015b).

To test the jet-driven outflow hypothesis, we compare the momentum flux of the atomic jet and the molecular outflow. Reiter et al. (2015b) estimated the jet mass-loss rate to be $\dot{M}_{\text{jet}} \gtrsim 5 \times 10^{-6}$ M$_\odot$ yr^{-1}, within a factor of a few of the mass-loss rate we find in the molecular outflow, $\dot{M}_{\text{out}} \gtrsim 1 \times 10^{-6}$ M$_\odot$ yr^{-1} (see Table 4). The faster jet velocity ($\sim$100 km s^{-1}) compared to the molecular outflow ($\sim$few km s^{-1}) leads to a difference of more than an order of magnitude in the momentum flux from the two components. If the jet mass-loss rate and therefore momentum are even higher, as suggested in Paper I, then the jet can readily entrain the molecular outflow (e.g. Raga & Cabrit 1993; Lee et al. 2000; Arce & Goodman 2001; Ostriker et al. 2001).

External irradiation from nearby O-type stars illuminates the atomic jet, revealing material between shock fronts that would be too cold to see in more quiescent regions. This unique view makes HH 900 one of only a few sources where the momentum flux of both the jet and the outflow can be measured. In addition to testing whether the jet may drive the molecular outflow (as discussed above), systems like this are valuable to constrain the relative contribution of fast, collimated atomic jets and molecu-

lar outflows to the momentum budget in embedded star-forming regions.

Using a sample of jets and outflows in NGC 1333, Dionatos & Güdel (2017) found that the momentum flux of molecular outflows exceeds that of atomic jets. For the HH 900 jet+outflow system, as for a larger sample of externally irradiated jets in Carina (Reiter et al. 2017), we find that atomic jets have comparable or larger momentum flux compared to molecular outflows. Reiter et al. (2017) determined the momentum flux in the atomic jet component of HH 900 to be $\log(\dot{P}) \approx -2.7$, although evidence for higher densities presented in Paper I suggests that this may be even greater. In Section 3.5, we computed a momentum flux in the cold molecular outflow of $\log(\dot{P}) \approx -4.1$ (taking the average of the red- and blueshifted lobes), remarkably similar to the momentum flux Reiter et al. (2017) estimate in the irradiated outflow [$\log(\dot{P}) \approx -4.3$]. Different methods of measuring the atomic jet component may lead to differences in the fraction of the total mass included in the momentum flux estimate (see Reiter et al. 2017).

5 COLD MOLECULAR GAS AND DUST IN THE TADPOLE-SHAPED GLOBULE

The ALMA data presented in this paper provide the first detection of the deeply embedded HH 900 YSO. Both Reiter et al. (2015b) and Paper I argue that high densities in the tadpole globule provide several magnitudes of extinction to obscure the HH 900 YSO. We can estimate the extinction to the HH 900 YSO from the molecular column density using the relationship between A_V and $N(^{13}\text{CO})$ derived by Dickman (1978)

$$A_{\text{v}} \approx (4.0 \pm 2.0) \times 10^{-16} \times N(^{13}\text{CO}) \text{ mag} \tag{5}$$

assuming LTE. Using the median optical-depth-corrected ^{13}CO column density, $N(^{13}\text{CO}) \sim 1.25 \times 10^{17}$ cm^{-2}, we find $A_{\text{V}} \sim 50$ mag.

This high A_V is consistent with a protostar too embedded to be seen at shorter wavelengths, but more than an order of magnitude higher than the $A_V \sim 2.5$ mag derived from optical hydrogen recombination lines in Paper I. However, the optical diagnostics only probe the extinction in front of the ionized layer on the globule surface. The higher A_V estimate from the $N(^{13}CO)$ includes the extinction from gas and dust in the tadpole globule itself, and thus reflects a much larger column of material.

The temperature structure of the globule shows evidence of the external influence of the environment (see Fig. 3 and Section 3.4). Multiple lines of evidence point to a positive radial temperature gradient with hotter gas near the surface of the globule compared to the interior (see Fig. 3 and Section 3.4). While the surface of the globule is hot and ionized (see Paper I), dust deep in the interior of the tadpole remains cold, with continuum emission better fitted with models with lower temperatures ($T < 30$ K; see Fig. 9 and Section 3.6). We serendipitously detect DCN J=3–2 in the centre of the globule, which we take as evidence that the gas is also cold (see Section 3.7). Chemical reactions in cold gas can enhance the abundance of deuterated species, especially in high-density gas where CO is depleted (e.g. Dalgarno & Lepp 1984; Millar, Bennett & Herbst 1989; Turner 2001). Where DCN has been detected in hot sources (e.g. Orion KL; Mangum, Plambeck & Wootten 1991), it is thought to have been returned to the gas phase from icy grain mantles only recently. Using the estimated dust mass surrounding the HH 900 YSO ($\sim 1\,M_\odot$; see Section 3.6) and assuming a uniform density profile, the average density in the globule is $\gtrsim 10^6$ cm^{-3}. This is well above the density where gas and dust are expected to be thermally coupled (see e.g. Goldsmith 2001; Galli, Walmsley & Gonçalves 2002). Together, this suggests cooler temperatures deep in the tadpole globule, where it is shielded from the harsh environment by the large column density of material.

5.1 Globule survival

In Paper I, we estimated that the tadpole is being photoevaporated at a rate of $\dot{M} \sim 5 \times 10^{-7}\,M_\odot$ yr^{-1}. Assuming a constant photo-evaporation rate, we can compute the remaining globule lifetime. We have estimated the mass in two different but complementary ways: (1) using $N(C^{18}O)$, assuming it is optically thin; and (2) from the dust continuum (see Section 3.6). Using $N(C^{18}O)$, we estimate the mass of molecular gas in the tadpole globule to be $\sim 0.6\,M_\odot$ (see Section 3.3). Given the high optical depths in the tadpole, it is likely that $C^{18}O$ is also optically thick, so this mass estimate is a lower limit. Continuum emission is the most optically thin diagnostic available. From the dust continuum, we estimate a mass of $M_{tadpole} \approx 1.9\,M_\odot$, a factor of ~ 3 higher than the estimate from $C^{18}O$ ($\sim 0.6\,M_\odot$) and roughly half the Bonnor–Ebert mass estimated in Paper I ($\sim 3.7\,M_\odot$). We note that the $C^{18}O$ and dust continuum trace different spatial distributions (see Figs 2 and 8), so the sum of the two masses may be a better reflection of the mass of the globule. In the following, we focus on the mass estimate from the dust continuum of the tadpole as a whole.

Assuming a constant photoevaporation rate, a $1.9\,M_\odot$ globule will be completely ablated in ~ 4 Myr. The remaining globule lifetime will be shorter (~ 1 Myr) or longer (~ 7 Myr; see Paper I) for the lower and higher mass estimates, respectively. For these remaining globule lifetimes, the HH 900 YSO will emerge into the H II region as the high-mass stars in nearby Tr16 explode as supernovae.

Fossil evidence in the Solar system meteorites requires that the Sun formed near at least one dying high-mass star (e.g. Adams 2010), suggesting that the tadpole provides an interesting

environment for planet formation. Although the planet formation process is still not fully understood, there is growing evidence that it happens early. For example, the concentric rings of HL Tau with an age of ~ 1 Myr (ALMA Partnership 2015) can be explained in terms of three embedded planets (Dipierro et al. 2015, although see Zhang, Blake & Bergin 2015). The pebble accretion-driven model of planet formation in the famous seven-planet hosting Trappist-1 system also operates on an ~ 1 Myr time-scale (Ormel, Liu & Schoonenberg 2017; Schoonenberg et al. 2019). Given that photoevaporation of planet-forming discs by other stars in a cluster can severely constrain planet formation even if planet formation happens early (e.g. Haworth et al. 2018; Winter et al. 2018; Concha-Ramírez et al. 2019; Nicholson et al. 2019) any progress towards planet formation in an embedded stage such as within a globule is very important.

Model fits to the continuum spectral index (see Section 3.6) suggest that grain growth is already underway in the tadpole. High optical depths and high densities in the globule shield the disc from the harsh radiative environment (as suggested by the positive radial temperature gradient; see Section 3.4). The inferred globule lifetime of ~ 4 Myr could in principle permit the entire planet formation process to take place while shielded from external irradiation from the nearby stellar cluster. Even the shortest estimated globule lifetime of ~ 1 Myr (which we consider to be an underestimate) would allow significant progress towards planet formation, for example through rapid grain growth and radial drift into small radii (e.g. Birnstiel, Klahr & Ercolano 2012), before the globule is completely ablated. As discussed in the previous paragraph, discs around young (~ 1 Myr) sources show rings and other characteristics thought to be due to planet formation (ALMA Partnership 2015). In this case, dense star-forming globules may be an important class of planet-forming systems in stellar clusters.

Disc evolution within this context may still differ from local clouds given the high optical depths and high densities in the tadpole. For example, if external feedback acts to accelerate the collapse of the globule, the disc accretion rate may also be enhanced, altering the dynamics in the planet-forming disc. It is unclear whether or how such star-forming globules may be enriched with the short-lived radioactive isotopes that play an important role in the geochemical evolution of terrestrial exoplanets (e.g. Grimm & McSween 1993). Recent studies point to pre-supernova mass-loss as an important source of short-lived elements (Lugaro, Ott & Keresztúri 2018) that may also provide an earlier enrichment pathway. Indeed, the current abundance of key elements like ^{26}Al in Carina appears to be of the order of the value inferred for the early Solar system (see discussion in Reiter & Parker 2019).

5.2 Globule kinematics

The ALMA data presented in this paper reveal the deeply embedded HH 900 YSO for the first time, providing unambiguous evidence for star formation in the opaque tadpole globule. Infalling gas often shows complex self-absorbed line profiles (e.g. Walker et al. 1986; Tafalla et al. 1998; Narayanan et al. 2002; Reiter et al. 2011); however, line profiles from the tadpole tend to be single peaked (see Fig. 4). Bright-rimmed clouds that have been affected by external feedback often do not show the asymmetric line profiles characteristic of infall (e.g. De Vries, Narayanan & Snell 2002; Thompson & White 2004). This absence has been attributed to other dynamical effects like rotation, pulsation, or a combination of collapse and expansion (e.g. Redman et al. 2004; Keto et al. 2006; Gao & Lou 2010; Wang, van der Tak & Hogerheijde 2012). In the

case of the tadpole, the positive radial thermal profile can explain the absence of characteristic line asymmetries: Hot intervening material does not absorb emission from the colder inner regions, and emission closer to the line peak traces warmer, more external gas (see Section 3.4).

P–V slices through the globule trace a C-shaped morphology (see Fig. 11 and Section 3.9). Tracers like $C^{18}O$ probe the kinematics of the colder gas deeper in the globule than optically thick lines like ^{13}CO. We expect that global motions will produce a similar morphology in the $C^{18}O$ P–V diagrams. While the shape of the emission in both lines is similar, it is not clear what kinematic structure this traces. C-shaped features have been seen in P–V profiles of ionized gas tracing much larger scales (e.g. Keto 2002; Keto & Wood 2006) and interpreted as infall. By fitting the profile for infall and rotation, Keto (2002) derived an infall velocity of $\sim$4.5 km s^{-1}. We do not see evidence for global rotation of the tadpole.

We estimate the free-fall velocity in the tadpole, $v_{ff} = \sqrt{2GM/r}$. For the dust mass computed in Section 3.6 ($\sim$1.9 M$_\odot$), we find $v_{ff} \sim 1.2$ km s^{-1} in the absence of any pressure support. This is similar to the velocity difference we observe between the centre and the edge of the tadpole (see Fig. 11). The estimated free-fall velocity will be lower ($v_{ff} \sim 0.7$ km s^{-1}) for the mass estimated from the $C^{18}O$ (0.6 M$_\odot$) or higher ($v_{ff} \sim 1.6$ km s^{-1}) for the Bonnor–Ebert mass derived in Paper I ($\sim$3.7 M$_\odot$). Mottram et al. (2013) found infall velocities (extrapolated to 1000 au) of $\sim$1 km s^{-1} from radiative transfer modelling of water emission lines seen in low-mass protostars, assuming a free-fall velocity profile. Other authors using similar methods on different lines and higher spatial resolution data (e.g. Di Francesco et al. 2001) find somewhat smaller velocities.

On the theoretical side, few studies exist that present spatially resolved gas kinematics. Haworth et al. (2013) simulated bright-rimmed clouds compressed by an external ionizing source, and produced synthetic observations of the J=2–1 transition of ^{12}CO, ^{13}CO, and $C^{18}O$. The simulated data were optimized for comparison with observations from the James Clerk Maxwell Telescope, a 15 m single-dish facility with a beam size of $\sim$22 arcsec at these frequencies, more than an order of magnitude larger than the synthesized beam size of our ALMA data. As a result, example clouds presented in that paper are $\sim$50$\times$ the size of the tadpole.

6 COMPARISON WITH SIMILAR OBJECTS

6.1 Other protostars in Carina

Two flattened, disc-like structures have been reported in Carina, both from protostars embedded in small globules like the tadpole (Mesa-Delgado et al. 2016). Both discs are small, marginally resolved with a 0″.03 × 0″.02 beam, yielding approximate disc radii of $\sim$60 au. A disc of similar size around the HH 900 YSO would be unresolved in our ALMA data.

The 229 GHz flux densities of the two disc detections in Mesa-Delgado et al. (2016) are 0.9 and 1.5 mJy, a factor of $\sim$4 lower than the flux density of the HH 900 YSO embedded in the tadpole. The HH 900 jet mass-loss rate is an order of magnitude higher than that of either of jets driven by the protostars in the Mesa-Delgado et al. (2016) study, suggesting that the higher flux might come from a more massive circumstellar disc.

6.2 Other globules

Globules are seen in many H II regions and have been studied at shorter wavelengths for decades (e.g. Bok 1948; Herbig 1974; Reipurth 1983). Several authors also note a tadpole-like morphology

(e.g. Brandner et al. 2000; Sahai, Morris & Claussen 2012b; Wright et al. 2012). Tails of ionized gas coming from these objects typically point away from the ionizing sources. Their morphology resembles the tear-drop shape of the nebulosity surrounding true proplyds (e.g. O'dell & Wen 1994; Johnstone, Hollenbach & Bally 1998). Indeed, the tadpole was originally identified as a candidate proplyd (Smith et al. 2003), despite what looked like two separate and oppositely directed tails. These tails have now been identified as the HH 900 jet+outflow system. Molecular line observations of the tadpole and other globules demonstrate that their masses are orders of magnitude higher than typical proplyds (e.g. Mann & Williams 2010; Sahai et al. 2012b, a; Mann et al. 2014, respectively).

Like other globules seen in H II regions, the tadpole is primarily seen in silhouette (Smith et al. 2010). Paper I summarizes the morphological clues that suggest that the globule lies in front of Tr16: (1) its v_{LSR} is blueshifted by $\sim$10 km s^{-1} compared to the v_{LSR} of Carina (see Section 3 and Rebolledo et al. 2016); (2) the tadpole tail is further blueshifted with respect to the head (see Fig. 2); (3) the ionization front on the globule surface is bright on both the side closest to and further from Tr16 (see Paper I); and (4) the opaque globule centre suggests minimal illumination on the near side. If the system does lie in front of Tr16, this may help explain the absence of a spatially resolved tail of ionized gas seen extending from the tadpole in the direction away from Tr16.

Globules may instead be the remnants of dust pillars where the high-density material at the head has separated from the more diffuse body (e.g. Hester et al. 1996; Ercolano & Gritschneder 2011). The tadpole may be one such pillar remnant that pointed towards Tr16. We observe a velocity gradient in the molecular emission along the tadpole, with material in the tail a few km s^{-1} bluer than in the head. Motion in the tail is not affected by the molecular outflow, which is redshifted on this side of the HH 900 YSO (see Figs 5, 12, and 11). The peculiar tail may be the remnants of high-density pillar spine, as seen in a few other pillars in Carina (e.g. Klaassen et al. 2020).

Gahm et al. (2007) identified many small globulettes in the Rosette Nebula with typical sizes of $\sim$2500 au, similar to the observed size of the tadpole. Using the same extinction estimate technique, Grenman & Gahm (2014) identified hundreds of globulettes in Carina, including the tadpole. Most observations of the molecular gas content of these small globules have been performed using single-dish facilities with beam sizes of $\sim$18–27 arcsec, an order of magnitude larger than the typical globulette size. Nevertheless, some trends have been found in the properties of the large globulettes observed in this way. Both Gahm et al. (2013) and Haikala et al. (2017), targeting the Rosette and Carina, respectively, find systematically higher masses than estimates from the extinction. Haikala et al. (2017) confirm that the globulettes in Carina are smaller, higher density, and tend to have higher linewidths than those in the Rosette.

Globules that show evidence for an embedded protostar provide the best comparison with the tadpole. Both Sahai et al. (2012a) and Haikala et al. (2017) observed another star-forming globule in Carina that contains the HH 1006 jet. Sahai et al. (2012a) demonstrated that the mass of molecular gas is too high ($\sim$350 M_{Jup}) for this object to be a proplyd. Extended linewings probably trace the molecular outflow associated with the HH 1006 jet (Reiter, Smith & Bally 2016). Haikala et al. (2017) also find that the linewidths in the HH 1006 globule are larger than those in globulettes without evidence for star formation. Like the HH 1006 globule, we find that the tadpole is more massive than previous estimates ($\sim$1.9 M$_\odot$; see Section 3.6). Broad linewidths, especially in ^{12}CO, reveal the molecular outflow associated with the HH 900 jet+outflow system

(see Fig. 6). The tadpole is too opaque to probe the circumstellar disc, unlike HH 1006 where Mesa-Delgado et al. (2016) estimated a disc mass of $\sim$27 $M_{\rm Jup}$ (assuming T=40 K) around the embedded protostar.

More detailed comparisons will be possible in the future as ALMA observes the internal structure of more of the globules in Carina and other H II regions.

7 CONCLUSIONS

We present spatially and spectrally resolved ALMA observations of a small globule, the tadpole, in the Carina Nebula. Previous observations at shorter wavelengths of the HH 900 jet+outflow system that emerges from the globule suggested a protostar and molecular outflow hidden in the opaque globule (see Reiter et al. 2015b and Paper I). Our ALMA data have angular resolution comparable to *HST*, allowing us to conduct a detailed analysis of the embedded protostar, molecular outflow, and tadpole globule as a whole. Our main conclusions are as follows:

(i) We detect the molecular outflow associated with the HH 900 jet+outflow system for the first time in ^{12}CO J=2–1. The wide-angle molecular outflow traces a biconical shape that joins smoothly with irradiated outflow seen outside the globule (Paper I).

(ii) The momentum flux in the HH 900 molecular outflow is comparable to that in the atomic jet, consistent with the jet-driven outflow morphology seen in the overall system.

(iii) The HH 900 YSO is detected on the jet axis inferred from optical and near-IR images, and is the clear origin of the associated molecular outflow. Continuum emission near the HH 900 YSO is marginally resolved, and appears to be slightly flattened perpendicular to the outflow axis. Optical depths in the globule are too high to trace the kinematics of the gas closest to the source. The serendipitous detection of DCN J=3–2 surrounding the HH 900 YSO suggests that gas in the centre of the globule remains cold, despite evidence that the harsh environment heats the globule surface to higher temperatures. The best-fitting continuum spectral index of $\sim$2 suggests that grain growth is already underway in the HH 900 YSO.

(iv) We measure high optical depths in the CO isotopologues, in line with previous estimates of high densities in the globule that render it opaque at shorter wavelengths.

(v) From the dust continuum emission, we estimate a globule mass of $\sim$1.9 M$_\odot$.

(vi) For the photoevaporation rate estimated in Paper I, this suggests that the remaining lifetime of the tadpole is $\sim$4 Myr. While external photoevaporation rapidly destroys protoplanetary discs around exposed stars, this long globule lifetime suggests that the HH 900 YSO will remain shielded from the environment for much of the planet formation time-scale. Evidence for grain growth in the tadpole suggests that dense globules may be an important class of planet-forming systems in stellar clusters.

(vii) P–V slices through the tadpole (perpendicular to the outflow) show a C-shape morphology in ^{13}CO and C^{18}O. This emission structure has been interpreted as infall when observed in other sources. Unlike colder sources where characteristic line asymmetries indicate infall, line profiles in the tadpole are remarkably symmetric. Whether gas kinematics in the tadpole are consistent with infall remains unclear.

The HH 900 YSO and jet+outflow system are clearly much younger than nearby Tr16. RDI may be an essential element of the dynamical evolution of the globule. A more thorough discussion of

how environment affects the kinematics and evolution of the globule will be presented in Paper III.

REFERENCES

Adams F. C., 2010, ARA&A, 48, 47
Adams F. C., Shu F. H., 1985, ApJ, 296, 655
ALMA Partnership, 2015, ApJ, 808, L3
Andrews S. M. et al., 2012, ApJ, 744, 162
Ansdell M. et al., 2018, ApJ, 859, 21
Arce H. G., Goodman A. A., 2001, ApJ, 554, 132
Arce H. G., Shepherd D., Gueth F., Lee C.-F., Bachiller R., Rosen A., Beuther H., 2007, Protostars and Planets V, University of Arizona Press, Tucson, p. 245
Astropy Collaboration, 2013, A&A, 558, A33
Bacciotti F., Mundt R., Ray T. P., Eislöffel J., Solf J., Camezind M., 2000, ApJ, 537, L49
Bacmann A., Lefloch B., Ceccarelli C., Castets A., Steinacker J., Loinard L., 2002, A&A, 389, L6
Bergin E. A., Tafalla M., 2007, ARA&A, 45, 339
Bertoldi F., 1989, ApJ, 346, 735
Bertoldi F., McKee C. F., 1992, ApJ, 395, 140
Birnstiel T., Klahr H., Ercolano B., 2012, A&A, 539, A148
Bisbas T. G., Wünsch R., Whitworth A. P., Hubber D. A., Walch S., 2011, ApJ, 736, 142
Bok B. J., 1948, Harv. Obs. Monogr., 7, 53
Boneberg D. M., Dale J. E., Girichidis P., Ercolano B., 2015, MNRAS, 447, 1341

[1]http://www.astropy.org

Brandner W. et al., 2000, AJ, 119, 292
Cabrit S., Bertout C., 1986, ApJ, 307, 313
Calvet N., Canto J., Rodriguez L. F., 1983, ApJ, 268, 739
Caselli P., Ceccarelli C., 2012, A&AR, 20, 56
Caselli P., Hartquist T. W., Havnes O., 1997, A&A, 322, 296
Codella C., Beltrán M. T., Cesaroni R., Moscadelli L., Neri R., Vasta M., Zhang Q., 2013, A&A, 550, A81
Codella C., Cabrit S., Gueth F., Cesaroni R., Bacciotti F., Lefloch B., McCaughrean M. J., 2007, A&A, 462, L53
Concha-Ramírez F., Wilhelm M. J. C., Portegies Zwart S., Haworth T. J., 2019, MNRAS, 490, 5678
Dale J. E., 2017, MNRAS, 467, 1067
Dale J. E., Bonnell I., 2011, MNRAS, 414, 321
Dale J. E., Ercolano B., Bonnell I. A., 2013, MNRAS, 431, 1062
Dalgarno A., Lepp S., 1984, ApJ, 287, L47
De Vries C. H., Narayanan G., Snell R. L., 2002, ApJ, 577, 798
Dickman R. L., 1978, ApJS, 37, 407
Di Francesco J., Myers P. C., Wilner D. J., Ohashi N., Mardones D., 2001, ApJ, 562, 770
Dionatos O., Güdel M., 2017, A&A, 597, A64
Dipierro G., Price D., Laibe G., Hirsh K., Cerioli A., Lodato G., 2015, MNRAS, 453, L73
Downes T. P., Cabrit S., 2007, A&A, 471, 873
Draine B. T., 2006, ApJ, 636, 1114
Dyson J. E., 1968, Ap&SS, 1, 388
Ercolano B., Gritschneder M., 2011, MNRAS, 413, 401
Ferreira J., 1997, A&A, 319, 340
Gahm G. F., Grenman T., Fredriksson S., Kristen H., 2007, AJ, 133, 1795
Gahm G. F., Persson C. M., Mäkelä M. M., Haikala L. K., 2013, A&A, 555, A57
Gaia Collaboration, 2016, A&A, 595, A1
Gaia Collaboration, 2018, A&A, 616, A1
Galli D., Walmsley M., Gonçalves J., 2002, A&A, 394, 275
Gao Y., Lou Y.-Q., 2010, MNRAS, 403, 1919
Gerner T., Shirley Y. L., Beuther H., Semenov D., Linz H., Albertsson T., Henning T., 2015, A&A, 579, A80
Goldsmith P. F., 2001, ApJ, 557, 736
Goldsmith P. F., Langer W. D., 1999, ApJ, 517, 209
Gómez-Ruiz A. I., Gusdorf A., Leurini S., Menten K. M., Takahashi S., Wyrowski F., Güsten R., 2019, A&A, 629, A77
Grenman T., Gahm G. F., 2014, A&A, 565, A107
Grimm R. E., McSween H. Y., 1993, Science, 259, 653
Gritschneder M., Burkert A., Naab T., Walch S., 2010, ApJ, 723, 971
Gritschneder M., Naab T., Walch S., Burkert A., Heitsch F., 2009, ApJ, 694, L26
Gusdorf A., Cabrit S., Flower D. R., Pineau Des Forêts G., 2008, A&A, 482, 809
Guzmán A. E., Garay G., Brooks K. J., Rathborne J., Güsten R., 2011, ApJ, 736, 150
Guzmán A. E. et al., 2014, ApJ, 796, 117
Haikala L. K., Gahm G. F., Grenman T., Mäkelä M. M., Persson C. M., 2017, A&A, 602, A61
Haworth T. J., Facchini S., Clarke C. J., Mohanty S., 2018, MNRAS, 475, 5460
Haworth T. J., Harries T. J., Acreman D. M., Rundle D. A., 2013, MNRAS, 431, 3470
Herbig G. H., 1974, PASP, 86, 604
Hester J. J. et al., 1996, AJ, 111, 2349
Johnstone D., Hollenbach D., Bally J., 1998, ApJ, 499, 758
Keene J., Schilke P., Kooi J., Lis D. C., Mehringer D. M., Phillips T. G., 1998, ApJ, 494, L107
Kessel-Deynet O., Burkert A., 2003, MNRAS, 338, 545
Keto E., 2002, ApJ, 568, 754
Keto E., Broderick A. E., Lada C. J., Narayan R., 2006, ApJ, 652, 1366
Keto E., Wood K., 2006, ApJ, 637, 850
Klaassen P. D., Johnston K. G., Leurini S., Zapata L. A., 2015, A&A, 575, A54

Klaassen P. D., Reiter M. R., McLeod A. F., Mottram J. C., Dale J. E., Gritschneder M., 2020, MNRAS, 491, 178
Lampton M., Margon B., Bowyer S., 1976, ApJ, 208, 177
Lee C.-F., Mundy L. G., Reipurth B., Ostriker E. C., Stone J. M., 2000, ApJ, 542, 925
Lefloch B., Cernicharo J., Reipurth B., Pardo J. R., Neri R., 2007, ApJ, 658, 498
Lefloch B., Lazareff B., 1994, A&A, 289, 559
Leurini S., Codella C., Gusdorf A., Zapata L., Gómez-Ruiz A., Testi L., Pillai T., 2013, A&A, 554, A35
Lugaro M., Ott U., Keresztluri Á., 2018, Prog. Part. Nucl. Phys., 102, 1
MacLaren I., Richardson K. M., Wolfendale A. W., 1988, ApJ, 333, 821
Mangum J. G., Plambeck R. L., Wootten A., 1991, ApJ, 369, 169
Mangum J. G., Shirley Y. L., 2015, PASP, 127, 266
Mann R. K., Williams J. P., 2010, ApJ, 725, 430
Mann R. K. et al., 2014, ApJ, 784, 82
Margulis M., Lada C. J., 1985, ApJ, 299, 925
McCaughrean M. J., Andersen M., 2002, A&A, 389, 513
McKee C. F., Ostriker E. C., 2007, ARA&A, 45, 565
McMullin J. P., Waters B., Schiebel D., Young W., Golap K., 2007, in Shaw R. A., Hill F., Bell D. J., eds, ASP Conf. Ser. Vol. 376, Astronomical Data Analysis Software and Systems XVI. Astron. Soc. Pac., San Francisco, p. 127
Mesa-Delgado A., Zapata L., Henney W. J., Puzia T. H., Tsamis Y. G., 2016, ApJ, 825, L16
Miao J., White G. J., Thompson M. A., Nelson R. P., 2009, ApJ, 692, 382
Millar T. J., Bennett A., Herbst E., 1989, ApJ, 340, 906
Mottram J. C., van Dishoeck E. F., Schmalzl M., Kristensen L. E., Visser R., Hogerheijde M. R., Bruderer S., 2013, A&A, 558, A126
Narayanan G., Moriarty-Schieven G., Walker C. K., Butner H. M., 2002, ApJ, 565, 319
Nicholson R. B., Parker R. J., Church R. P., Davies M. B., Fearon N. M., Walton S. R. J., 2019, MNRAS, 485, 4893
Ohlendorf H., Preibisch T., Gaczkowski B., Ratzka T., Grellmann R., McLeod A. F., 2012, A&A, 540, A81
Ormel C. W., Liu B., Schoonenberg D., 2017, A&A, 604, A1
Orozco-Aguilera M. T., Zapata L. A., Hirota T., Qin S.-L., Masqué J. M., 2017, ApJ, 847, 66
Ossenkopf V., Henning T., 1994, A&A, 291, 943
Ostriker E. C., Lee C.-F., Stone J. M., Mundy L. G., 2001, ApJ, 557, 443
Oya Y., Sakai N., López-Sepulcre A., Watanabe Y., Ceccarelli C., Lefloch B., Favre C., Yamamoto S., 2016, ApJ, 824, 88
O'dell C. R., Wen Z., 1994, ApJ, 436, 194
Pickett H. M., Poynter R. L., Cohen E. A., Delitsky M. L., Pearson J. C., Müller H. S. P., 1998, J. Quant. Spectrosc. Radiat. Transfer, 60, 883
Pottasch S. R., 1956, Bull. Astron. Inst. Neth., 13, 77
Pottasch S. R., 1958, Bull. Astron. Inst. Neth., 14, 29
Povich M. S. et al., 2011, ApJS, 194, 14
Price-Whelan A. M. et al., 2018, AJ, 156, 123
Pudritz R. E., Norman C. A., 1986, ApJ, 301, 571
Pyo T.-S. et al., 2003, ApJ, 590, 340
Raga A., Cabrit S., 1993, A&A, 278, 267
Rebolledo D. et al., 2016, MNRAS, 456, 2406
Redman M. P., Keto E., Rawlings J. M. C., Williams D. A., 2004, MNRAS, 352, 1365
Reipurth B., 1983, A&A, 117, 183
Reiter M., Kiminki M. M., Smith N., Bally J., 2017, MNRAS, 470, 4671
Reiter M., McLeod A. F., Klaassen P. D., Guzmán A. E., Dale J. E., Mottram J. C., Garay G., 2019, MNRAS, 490, 2056
Reiter M., Parker R. J., 2019, MNRAS, 486, 4354
Reiter M., Shirley Y. L., Wu J., Brogan C., Wootten A., Tatematsu K., 2011, ApJ, 740, 40
Reiter M., Smith N., Bally J., 2016, MNRAS, 463, 4344
Reiter M., Smith N., Kiminki M. M., Bally J., 2015a, MNRAS, 450, 564
Reiter M., Smith N., Kiminki M. M., Bally J., Anderson J., 2015b, MNRAS, 448, 3429
Reiter M. et al., 2020, MNRAS, submitted

Remijan A. et al., 2019, ALMA Technical Handbook, ALMA Doc. 7.3, Ver. 1.0

Roberts H., Fuller G. A., Millar T. J., Hatchell J., Buckle J. V., 2002, A&A, 381, 1026

Robitaille T., Bressert E., 2012, APLpy: Astronomical Plotting Library in Python. Astrophysics Source Code Library, record ascl:1208.017

Roccatagliata V., Preibisch T., Ratzka T., Gaczkowski B., 2013, A&A, 554, A6

Sahai R., Güsten R., Morris M. R., 2012a, ApJ, 761, L21

Sahai R., Morris M. R., Claussen M. J., 2012b, ApJ, 751, 69

Schilke P., Walmsley C. M., Pineau des Forets G., Flower D. R., 1997, A&A, 321, 293

Schneps M. H., Ho P. T. P., Barrett A. H., 1980, ApJ, 240, 84

Schoonenberg D., Liu B., Ormel C. W., Dorn C., 2019, A&A, 627, A149

Schöier F. L., van der Tak F. F. S., van Dishoeck E. F., Black J. H., 2005, A&A, 432, 369

Smith N., 2006, ApJ, 644, 1151

Smith N., Bally J., Morse J. A., 2003, ApJ, 587, L105

Smith N., Bally J., Walborn N. R., 2010, MNRAS, 405, 1153

Smith N., Barbá R. H., Walborn N. R., 2004, MNRAS, 351, 1457

Tafalla M., Mardones D., Myers P. C., Caselli P., Bachiller R., Benson P. J., 1998, ApJ, 504, 900

Thompson M. A., White G. J., 2004, A&A, 419, 599

Tobin J. J., Hartmann L., Chiang H.-F., Wilner D. J., Looney L. W., Loinard L., Calvet N., D'Alessio P., 2012, Nature, 492, 83

Tobin J. J. et al., 2015, ApJ, 805, 125

Tremblin P. et al., 2013, A&A, 560, A19

Turner B. E., 2001, ApJS, 136, 579

van Kempen T. A. et al., 2009, A&A, 507, 1425

Walch S., Whitworth A. P., Bisbas T. G., Wünsch R., Hubber D. A., 2013, MNRAS, 435, 917

Walker C. K., Lada C. J., Young E. T., Maloney P. R., Wilking B. A., 1986, ApJ, 309, L47

Wang K. S., van der Tak F. F. S., Hogerheijde M. R., 2012, A&A, 543, A22

Wilson T. L., 1999, Rep. Prog. Phys., 62, 143

Winter A. J., Clarke C. J., Rosotti G., Ih J., Facchini S., Haworth T. J., 2018, MNRAS, 478, 2700

Wright N. J., Drake J. J., Drew J. E., Guarcello M. G., Gutermuth R. A., Hora J. L., Kraemer K. E., 2012, ApJ, 746, L21

Yıldız U. A., Kristensen L. E., van Dishoeck E. F., Belloche A., van Kempen T. A., Hogerheijde M. R., Güsten R., van der Marel N., 2012, A&A, 542, A86

Zhang K., Blake G. A., Bergin E. A., 2015, ApJ, 806, L7

APPENDIX A: COORDINATE CORRECTION OF ACS/*HST* IMAGE

For this work, we corrected the coordinates of the ACS/*HST* Hα (F658N filter) image taken on 2005 July 18 (Smith et al. 2010) by comparing this image with the position of 23 *Gaia* sources in the field (Gaia Collaboration 2016, 2018). Fig. A1 shows these sources and the position of each associated *Gaia* source by the time of the ACS/*HST* observations according to their proper motion. Panel (a) marks the position of the *Gaia* coordinates in the original Hα image. It is apparent that the *HST* coordinate solution is displaced on average by about $(\Delta\alpha, \Delta\delta) = (-0\!''\!.12, -0\!''\!.05)$, determined by comparing the peak position of the *HST* sources with the *Gaia* coordinates. Panel (b) shows Hα image with this correction applied. The centred Hα image shown in Fig. 1 is used to correct the [Fe II] image in Fig. 5. We consider this simple coordinate correction sufficiently accurate for the purpose of this study.
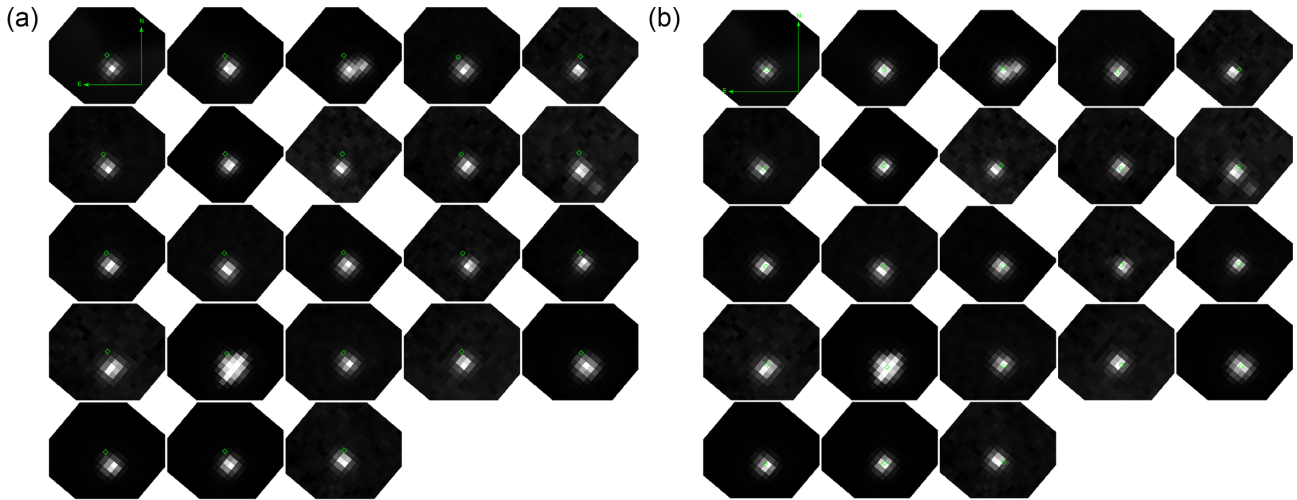
Figure A1. *HST*/ACS Hα image around *Gaia* sources in the field. Panel (a) shows *Gaia* sources' positions as green diamonds compared with the original ACS/*HST* image. Panel (b) shows the same but on to the image with corrected coordinates.
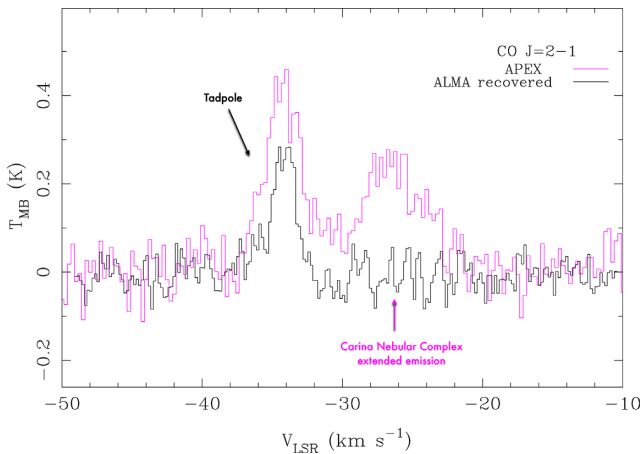
Figure B1. Comparison between the main-beam-corrected spectrum of the CO $J=2$–1 line towards HH 900 taken using APEX and the emission recovered by ALMA.

APPENDIX B: MAXIMUM RECOVERABLE SCALE. SHORT-BASELINE FILTERING

We evaluate how much ALMA recovers the large-scale emission from the tadpole. For that, we compare the ALMA data with the emission measured with the APEX telescope (project O-097.F-9337A.2016) of the CO $J=2$–1 towards HH 900. Position switching spectra were taken towards the tadpole position on 2016 April 4, integrating on-source ≈24 min, allowing us to reach an rms of 0.04 K main-beam-corrected temperature ($\eta_{MB} = 0.7$). The main beam FWHM of APEX at the CO $J=2$–1 frequency is 26$''$3. We weight the ALMA primary-beam-corrected CO $J=2$–1 line cube (natural weighting) with a 2D Gaussian of FWHM equivalent to the APEX main-beam size. This results in the black spectrum shown in Fig. B1. This spectrum is very similar to that obtained just by integrating the entire ALMA cube because the APEX telescope has the same diameter as the ALMA main array antennae.

The APEX spectrum in Fig. B1 shows two main components. There is a 3.2 km s^{-1}-wide component centred at -34.2 km s^{-1} and likely associated with the tadpole. A second component is 5.7 km s^{-1} wide and it is centred at -26.5 km s^{-1}. This second component is probably associated with the Carina Nebular Complex large-scale emission (Rebolledo et al. 2016; Klaassen et al. 2020).

Fig. B1 indicates that our ALMA observations recover approximately a 70 per cent from the tadpole emission. If this difference is real (in contrast to being artificially produced by, for example, calibration problems) and is due to interferometer short-baseline filtering, then the filtered emission should consist of an extended diffuse molecular envelope encompassing the tadpole. As expected, our ALMA observations cannot recover the widespread Carina Nebular emission from the second component.

APPENDIX C: PCYC 838

We detect continuum emission and CO from the YSO that lies in western limb of the outflow, PCYC 838 (see Figs 1 and 2). We do not detect ^{13}CO at the location of PCYC 838, so we assume that the ^{12}CO emission is optically thin. We use this to compute a median log$[N(CO)_{thin}]=15.9$ for PCYC 838, significantly lower than that estimated for the tadpole globule (see Table 3).

Table C1 gives the flux densities within a radius of 0$''$3 ($r_0 = 690$ au) of PCYC 838 and the spectral index of a power-law fit. The mass derived from the continuum fluxes (Table 5) towards PCYC 838 using the same hypotheses as in Section 3.6 is about 0.2 M$_\odot$, assuming 15 K. The stellar mass estimated by Povich et al. (2011) is $\sim$2.5 M$_\odot$ based on model fits to the SED. Because this source is visible at optical wavelengths, it is likely less embedded and it may be associated with a higher dust temperature. Assuming $T_{dust} = 50$ K, we obtain a mass of 0.05 M$_\odot$. The spectral index of the continuum emission towards PCYC 838 is also low, suggesting dust coagulation in this source, as in the HH 900 YSO. Unlike the HH 900 YSO, PCYC 838 is unresolved at all wavelengths.

Table C1. Position and flux densities of PCYC 838.

Source	R.A. (J2000)	Decl. (J2000)	217.1 GHz (mJy)	232.2 GHz (mJy)	331.6 GHz (mJy)	343.0 GHz (mJy)	α^a
PCYC 838	10:45:18.798	-59:44:23.78	1.21	1.44	2.64	2.73	1.8 ± 0.5

*Note.* ^{a}Spectral index of best power-law fit to flux densities ($S_\nu \propto \nu^\alpha$).
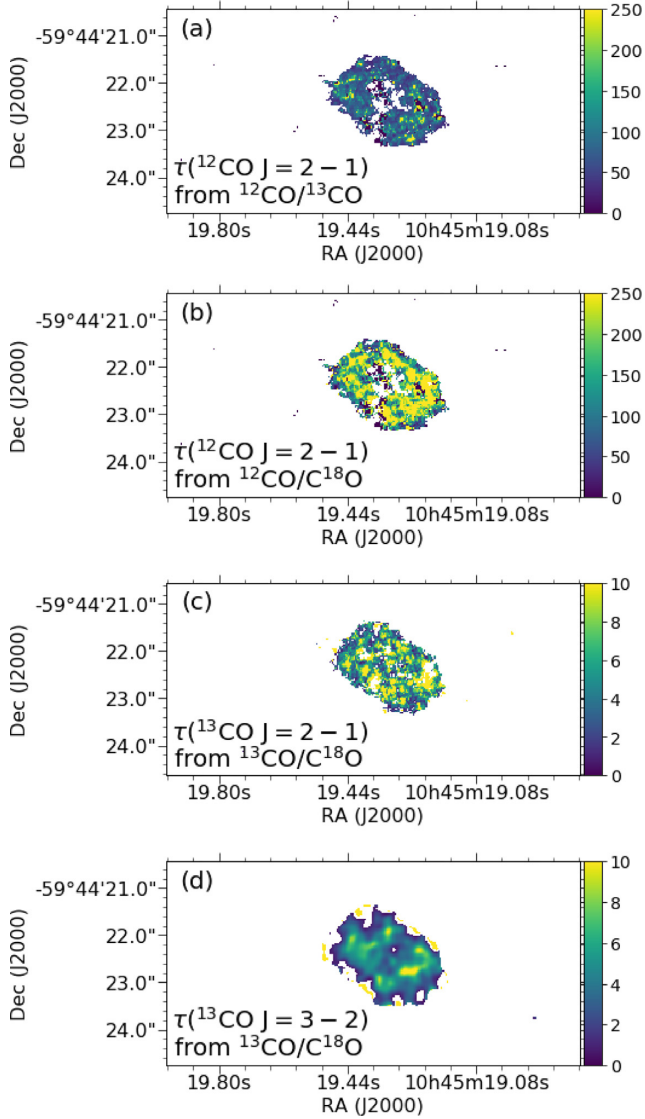
Figure D1. Maps of the optical depth, τ_v, of the (a) ^{12}CO J=2–1 from the temperature ratio T_{12}/T_{13}, (b) ^{12}CO J=2–1 from the temperature ratio T_{12}/T_{18}, (c) ^{13}CO J=2–1, and (d) ^{13}CO J=3–2. We compute τ for each pixel as a function of velocity; maps shown here display the value of τ_v at the $v_{\text{LSR}} = -33.5$ km s^{-1}.

APPENDIX D: OPTICAL DEPTH MAPS

As described in Section 3.1, we compute the optical depth at each position and at each velocity. We show maps of τ at the v_{LSR} in Fig. D1 to give an overview of the optical depth structure in the source. Data used in each calculation were masked for significance using the following cuts: 6σ for ^{12}CO, 4σ for ^{13}CO, and 3σ for C^{18}O. Maps shown reflect a single channel. As a result, not every pixel meets the significance threshold leading to white space in a few places in the maps shown in Fig. D1.

APPENDIX E: TEMPERATURE MAPS

We show a map of the peak brightness temperature of all of the observed CO isotopologues in Fig. E1. The brightness temperature depends on the excitation temperature as $T_{\text{mb}} = T_{\text{ex}}(1 - e^{-\tau})$. For optically thick lines ($\tau > >1$) $T_{\text{mb}} \approx T_{\text{ex}}$, allowing the brightness
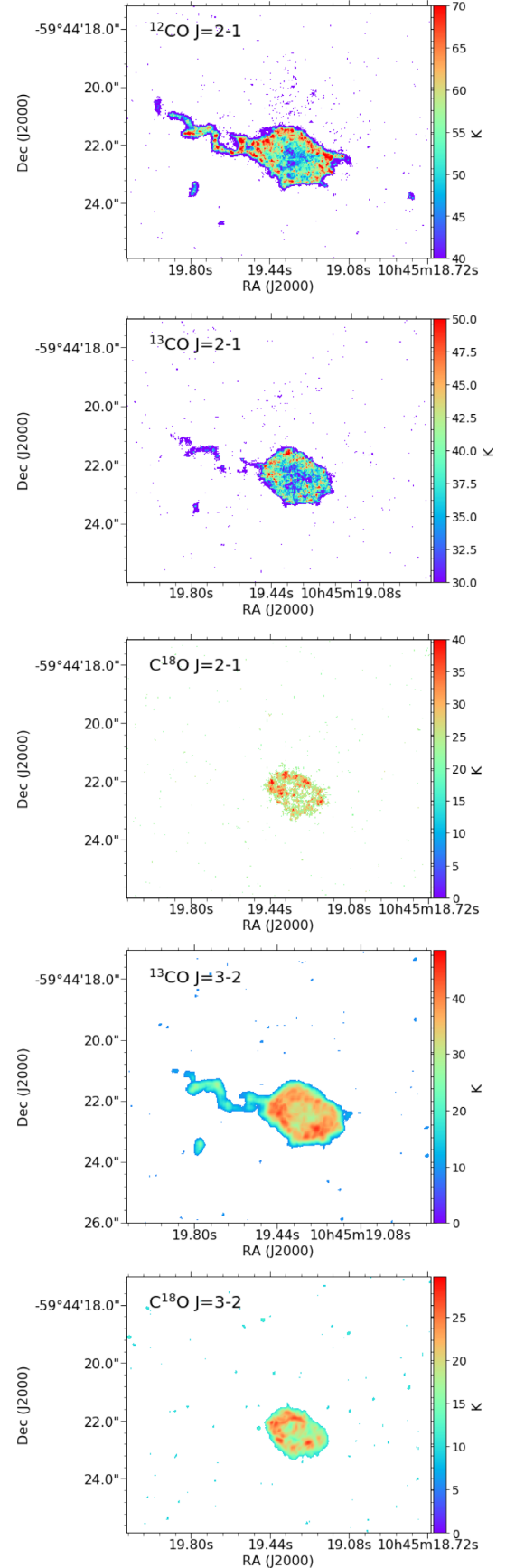
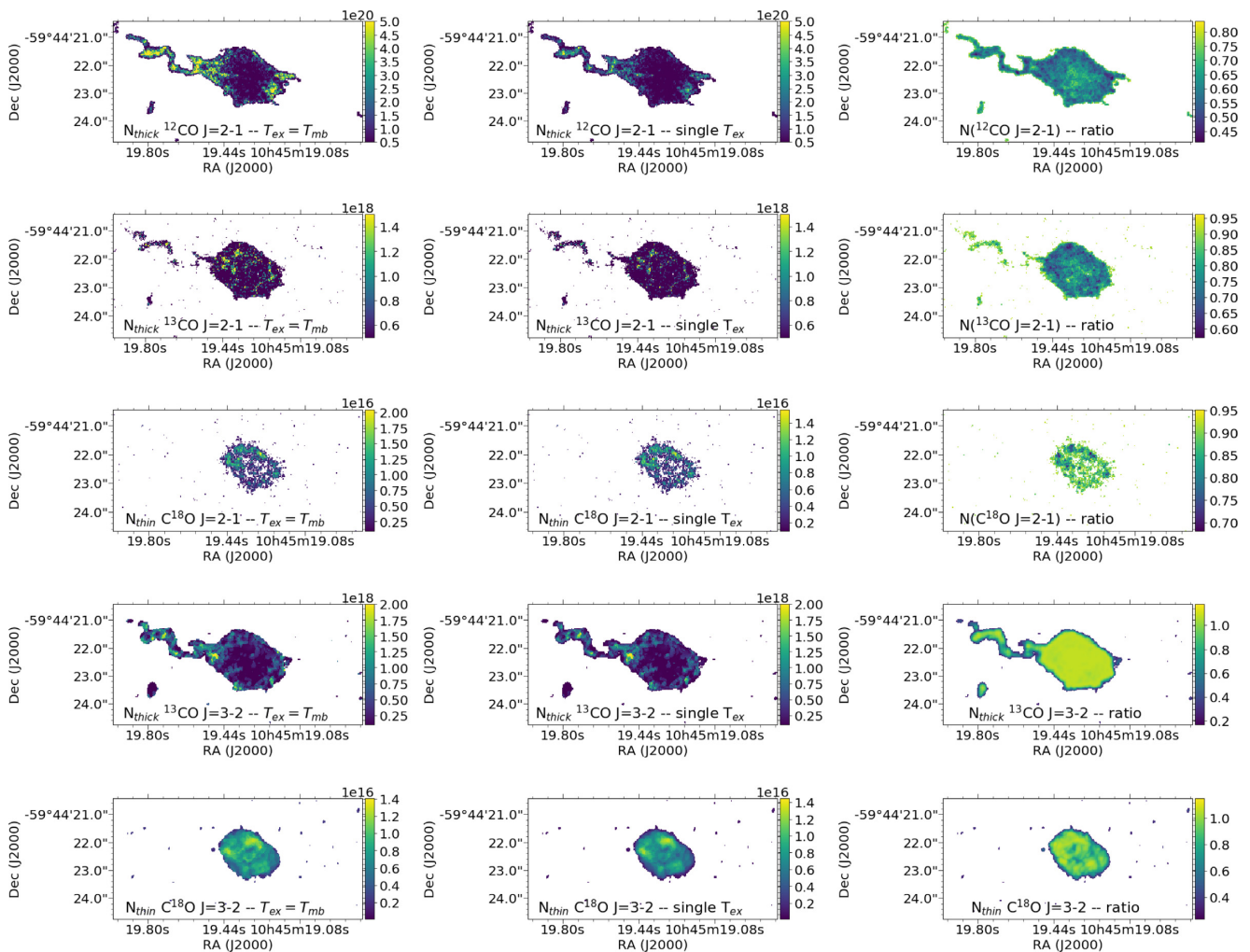**Figure E1.** Maps of the peak brightness temperature of all observed CO isotopologues.

temperature to be taken as a proxy for the excitation temperature (see also the discussion in Section 3.4). Assuming that all of the observed CO isotopologues are optically thick (see Section D and Fig. D1), the peak brightness temperatures shown in Fig. E1 reflect the excitation temperature of that line at the $\tau = 1$ surface.

The $\tau = 1$ surface traced by rarer isotopologues and higher excitation transitions should probe deeper in the cloud than the most abundant isotopologue (and most optically thick line), ^{12}CO J=2–1 (see Fig. 3). While our data do not allow us to constrain the location of the $\tau = 1$ surface, we note that the brightness temperature is lower for rarer isotopologues and higher excitation transitions.

APPENDIX F: COLUMN DENSITY MAPS

We show maps of the column density of the CO isotopologues in Fig. F1. In Section 3.2, we compute the column density assuming

a single excitation, $T_{ex} = 20$ K and argue that higher excitation temperatures will change this estimate by factors of $\sim$2. To confirm this, we recompute the column density of the CO lines assuming that the brightness temperature traces the excitation (i.e. using the temperature structure shown in Fig. E1). To compute the appropriate $Q(T_{ex})$ at each position, we take the discrete values of $Q(T_{ex})$ for each isotopologue given in the JPL Spectral Line Catalog (Pickett et al. 1998) and fit a third-order polynomial. Column densities computed this way are shown in the left column of Fig. F1. We compare this with the column densities we estimate assuming a single T_{ex} (shown in the middle column of Fig. F1). The ratio of the two column density calculations is shown in the right column of Fig. F1; values typically vary by a factor of $\lesssim$2.

Figure F1. Maps of the column density of all observed transitions of CO and its isotopologues. In the left column, we show the column density computed using the brightness temperature (see Section E and Fig. E1) as a proxy for excitation temperature (see Section 3.4). The centre column shows the column density assuming a single excitation temperature, $T_{ex} = 20$ K, as in Section 3.2. The right column shows the ratio of the two column density estimates (single T_{ex}/variable T_{ex}).

This paper has been typeset from a TeX/LaTeX file prepared by the author.